JGR Space Physics

RESEARCH ARTICLE
10.1029/2019JA027734

On the Production of Ionospheric Irregularities Via Kelvin-Helmholtz Instability Associated with Cusp Flow Channels

Andres Spicher[1], Kshitija Deshpande[2], Yaqi Jin[1], Kjellmar Oksavik[3,5], Matthew D. Zettergren[2], Lasse B. N. Clausen[1], Jøran I. Moen[1,5], Marc R. Hairston[4], and Lisa Baddeley[3,5]

[1]Department of Physics, University of Oslo, Oslo, Norway, [2]Department of Physical Sciences and Center for Space and Atmospheric Research (CSAR), Embry-Riddle Aeronautical University, Daytona Beach, Florida, USA, [3]Birkeland Centre for Space Science, Department of Physics and Technology, University of Bergen, Bergen, Norway, [4]Center for Space Sciences, University of Texas at Dallas, Richardson, Texas, USA, [5]University Centre in Svalbard, Longyearbyen, Norway

Abstract We present a multi-instrument multiscale study of a channel of enhanced, inhomogeneous flow in the cusp ionosphere occurring on November 30, 2014. We provide evidence that strong Global Navigation Satellite System (GNSS) phase scintillations indices ($\sigma_\phi > 0.5$ rad) can arise from such events, indicating that they are important in the context of space weather impacts on technology. We compare in detail two-dimensional maps of ionospheric density, velocity, and temperatures obtained by the European Incoherent Scatter Scientific Association Svalbard Radar with scintillation indices detected from a network of four GNSS receivers around Svalbard and examine the different sources of free energy for irregularity creation. We observe that the strongest phase scintillations occur on the poleward side of the flow channel in a region of sheared plasma motion and structured low-energy particle precipitation. As inhomogeneous plasma flows are evident in our observations, we perform a quantitative, nonlinear analysis of the Kelvin–Helmholtz instability (KHI) and its impact on phase scintillations using numerical simulations from the first principles-based Geospace Environment Model of Ion-Neutral Interactions and Satellite-beacon Ionospheric-scintillation Global Model of the upper Atmosphere. Using representative values consistent with the radar data, we show that KHI can efficiently create density structures along with considerable scintillations and is thus likely to contribute significantly under similar conditions, which are frequent in the cusp.

Key Points:
- Observations and modelling work document that cusp flow shears can give rise to strong phase scintillations
- The strongest phase scintillations occur in a region with inhomogeneous plasma flow and structured low-energy particle precipitation
- Simulations show strong correlation between phase scintillations and turbulent structures from KHI, especially with high capacitance

Supporting Information:
- Supporting Information S1
- Movie S1
- Movie S2

Correspondence to:
A. Spicher,
andres.spicher@fys.uio.no

Citation:
Spicher, A., Deshpande, K., Jin, Y., Oksavik, K., Zettergren, M. D., Clausen, L. B. N., et al. (2020). On the production of ionospheric irregularities via Kelvin-Helmholtz instability associated with cusp flow channels. *Journal of Geophysical Research: Space Physics*, *125*, e2019JA027734. https://doi.org/10.1029/2019JA027734

Received 27 DEC 2019
Accepted 24 MAR 2020
Accepted article online 7 APR 2020

1. Introduction

The ionospheric cusps are complex systems where highly dynamic phenomena occur due to their coupling to the solar wind, the magnetosphere, and the thermosphere. These phenomena include electron and ion precipitation, electrostatic and electromagnetic waves, and turbulence (e.g., Cargill et al., 2005; Carlson, 2012; Chaston et al., 2007; Heppner et al., 1993; Kelley & Carlson, 1977; Keskinen & Ossakow, 1983; Spicher et al., 2015, and references herein). At F region altitudes, this results in ionospheric density irregularities and turbulence, which are important for applications related to adverse effects of space weather on technology, as they can affect high-frequency (HF) communication and cause amplitude and phase scintillations of transionospheric radio signals such as the ones used by Global Navigation Satellite Systems (GNSS) (e.g., Carlson, 2012; Hey et al., 1946; Jin et al., 2019; Kintner & Seyler, 1985; Kintner et al., 2007; Moen et al., 2013; Phelps & Sagalyn, 1976; Prikryl et al., 2011; Spicher et al., 2015; Tsunoda, 1988; Wernik et al., 2003; Yeh & Liu, 1982). With increased human activity in the Arctic, making progress at identifying and understanding the physical mechanisms that create these ionospheric irregularities, which can range from a few decameters to a few tens of kilometers, is of growing importance.

At high latitudes, several possible sources of free energy and instability mechanisms exist, and three categories have gained significant attention (e.g. Carlson, 2012; Keskinen & Ossakow, 1983; Kintner & Seyler, 1985; Moen et al., 2013; Oksavik et al., 2011; Tsunoda, 1988; Wernik et al., 2003): (a) convective instabilities associated with density gradients (e.g., Keskinen & Ossakow, 1983; Tsunoda, 1988), (b) particle precipitation-driven irregularities (e.g., Dyson & Winningham, 1974; Keskinen & Ossakow, 1983), and (c)

flow shear-related instabilities (e.g., Ganguli et al., 1994; Heppner et al., 1993; Keskinen et al., 1988; Kintner & Seyler, 1985). In particular, the gradient drift instability (GDI) operating on polar cap patches is often regarded as a dominant process for the creation of density irregularities (e.g., Basu et al., 1988, 1994; Forsythe & Makarevich, 2018; Gondarenko & Guzdar, 2004; Lamarche & Makarevich, 2017; Linson & Workman, 1970; Makarevich, 2014, 2017; Oksavik et al., 2012; Simon, 1963; Tsunoda, 1988; Weber et al., 1984).

Particle precipitation is also believed to play an important role for plasma structuring in the cusp region (Dyson & Winningham, 1974; Kelley et al., 1982; Keskinen & Ossakow, 1983, and reference therein). Indeed, low-energy ($\leq$ 1,000 eV) precipitating electrons deposit most of their energy at F-region altitudes and might be a source of density perturbations for large to medium scale irregularities ($\lambda \geq 10$ km) (Dyson & Winningham, 1974; Kelley et al., 1982; Labelle et al., 1989; Millward et al., 1999; Rees, 1963). Moen et al. (2012) and Oksavik et al. (2012) suggested that the GDI could then further structure plasma gradients that were initially created by precipitation. Furthermore, Moen et al. (2002) hypothesized that the initial source of the decameter-scale perturbations associated with HF backscatter in the cusp might be the fine structures within particle precipitation itself.

Another source of energy can be found in flow shears, which are commonly found in the high latitude ionosphere in connection with discrete auroral forms (e.g., Moen et al., 2008; Oksavik et al., 2004a, 2005; Rinne et al., 2007). A relation between sheared plasma flow (inhomogeneous electric field) and broadband electrostatic turbulence and irregularities has been observed using rockets, satellites, and from the ground (e.g., Basu et al., 1986, 1988; Earle et al., 1989; Heppner et al., 1993; Kelley & Carlson, 1977; Oksavik et al., 2004b, 2011, 2012; Spicher et al., 2016). Shears in the cross-field ion velocity can initiate the Kelvin–Helmholtz instability (KHI) (Keskinen et al., 1988), a mechanism regarded as important for the creation of irregularities in the cusp (Basu et al., 1988, 1994; Oksavik et al., 2011), and on which, for instance, the GDI (Carlson et al., 2007) or microscale instabilities (Ganguli et al., 1994) could develop and further structure the plasma. One specific cusp phenomenon where cross-field sheared plasma flows and particle precipitation are fundamental is the reversed flow event (RFE) (Moen et al., 2008; Rinne et al., 2007). RFEs are latitudinally narrow ($\sim$ 50 to $\sim$ 250 km) and longitudinally extended ($> 400 - 600$ km) flow channels with flow direction opposite to that of the large-scale background convection (Rinne et al., 2007). They are common cusp features typically observed around magnetic noon and have a preference for interplanetary magnetic field (IMF) $|B_y| > |B_z|$ (Moen et al., 2008; Oksavik et al., 2011; Rinne et al., 2007). RFEs are believed to be signatures of a flux transfer event (FTE) (Southwood, 1987) and are related to the brightening of Birkeland current arcs (Moen et al., 2008; Oksavik et al., 2004a, 2005). Decameter-scale density irregularities have been observed in relation to RFEs, and it was proposed that the KHI and microscales instabilities could be responsible for their creation (e.g., Carlson et al., 2007; Oksavik et al., 2011; Spicher et al., 2016). RFEs are therefore cusp phenomena that are particularly interesting in the framework of space weather and flow shear instabilities (Moen et al., 2013).

Space weather studies based on ground-based GNSS data at high latitudes are numerous and include (not inclusive) statistical surveys (e.g., Alfonsi et al., 2011; Jin et al., 2018b; Prikryl et al., 2011, 2015; Spogli et al., 2009) and studies targeting specific ionospheric phenomena such as polar cap patches (e.g., Jin et al., 2014, 2016; Mitchell et al., 2005; van der Meeren et al., 2015; Zhang et al., 2017), the storm-enhanced density (SED)/tongue of ionization (TOI) (e.g., van der Meeren et al., 2014; Wang et al., 2016, 2018), auroral blobs (Jin et al., 2014, 2016), periods of extended dayside reconnection (Clausen et al., 2016), cusp aurora (poleward auroral moving forms) (Jin et al., 2015; Oksavik et al., 2015), auroral arcs (e.g., Forte et al., 2017; Semeter et al., 2017; van der Meeren et al., 2016), and cusp dynamics with or without polar cap patch production (Jin et al., 2017). However, despite the significant amount of studies, the physical causes for the development of the small-scale irregularities and associated enhanced scintillation observed are still not clear. In particular, the applicability and importance of different instability modes (e.g., KHI) in the high-latitude ionosphere remains to be tested.

Here, we present a multi-instrument multiscale study of a cusp flow channel (including an RFE) identified using the European Incoherent Scatter Scientific Association (EISCAT) Svalbard Radar (ESR) and leading to enhanced phase scintillations. Then, as velocity shears are evident in our data and due to the prevalence of inhomogeneous flows near the cusp (e.g., Carlson et al., 2008; Clauer, 2003; Heppner et al., 1993; Moen et al., 2008; Oksavik et al., 2004b, 2005; Rinne et al., 2007) where phase scintillations peak (Jin et al., 2015, 2017; Prikryl et al., 2015), we place our observations in the context of the KHI process. We do not intend

to rule out GDI or precipitation (or alternative possibilities) as playing a role in the scintillation for the specific event however, our main motivation is to test KHI and its impact on scintillations. Thus, we perform a quantitative, nonlinear analysis of KHI using numerical simulations from the Geospace Environment Model of Ion-Neutral Interactions (GEMINI) and Satellite-beacon Ionospheric-scintillation Global Model of the upper Atmosphere (SIGMA) and examine and discuss its potential role in creating cusp ionospheric irregularities and scintillations.

2. Instrumentation and Numerical Models

In this study, the large-scale context is obtained from the Super Dual Auroral Radar Network (SuperDARN) (Chisham et al., 2007) and Global Positioning System (GPS) Madrigal total electron content (TEC) maps (Rideout & Coster, 2006; Vierinen et al., 2016), while data from ESR (Wannberg et al., 1997) and from the Defense Meteorological Satellite Program (DMSP) F17 (Hairston, 2019; Redmon et al., 2017) provide details about the mesoscale structures. Irregularities smaller than a few kilometers are considered using GNSS data obtained from a network of four receivers around Svalbard (Oksavik et al., 2015) and SuperDARN spectral width observations (Chisham et al., 2007; Kintner et al., 2007). Furthermore, numerical simulations are performed to supplement the observations. The different instruments and models used are briefly presented in this section.

For completeness, we first briefly describe the solar wind conditions around the time of the event, that is, around 09:37 UT to 10:00 UT on November 30, 2014. This includes the IMF in geocentric solar magnetospheric coordinates (GSM), the solar wind velocity, and the proton density from the 1-min resolution OMNI data set (King & Papitashvili, 2005). The quantities have already been shifted to the observation site from the nose of the Earth's bow shock (King & Papitashvili, 2005).

We use SuperDARN data to map the large-scale context surrounding the mesoscale flow channels detected by the ESR. We present velocity vectors derived by merging data from the Hankasalmi and Pykkvibær radars. The line-of-sight velocity data from both radars are mapped onto an equal-area grid in the vicinity of the ESR field of view and aggregated over 6 min, as a compromise between data coverage and temporal resolution. Line-of-sight flow measurements within one grid cell are merged to form a two-dimensional (2D) flow vector, whenever both radars contribute (e.g., Ruohoniemi et al., 1989). The spectral width is computed in a similar manner.

We use data from four NovAtel GPStation-6 GNSS Ionospheric Scintillation and TEC Monitors installed in the Svalbard archipelago. The receivers are located in Ny-Ålesund (NYA; 78.9° N, 11.9° E), at the Kjell-Henriksen Observatory in Longyearbyen (LYB; 78.1° N, 16.0° E), in Hopen (HOP; 76.5° N, 25.0° E), and on Bear Island (BJN; 74.5° N, 19.0° E) (van der Meeren et al., 2015). The receivers are operated by the University of Bergen and track signals at several frequencies from GPS, GLONASS, and Galileo (Oksavik et al., 2015). The receivers output the phase scintillation index σ_ϕ (Fremouw et al., 1978; Rino, 1979), which is computed over 60 s from the raw carrier phase and detrended using a sixth-order Butterworth high-pass filter with the conventional frequency of 0.1 Hz (Van Dierendonck et al., 1993). The 60-s amplitude scintillation index S_4 (Briggs & Parkin, 1963), the TEC, and the rate of change of TEC (ROT) are also provided (Oksavik et al., 2015).

It is worth noting that σ_ϕ is not without issues. The index is sensitive to the cutoff frequency (0.1 Hz), which may include refractive contributions from larger-scale irregularities at high latitudes (e.g., Beach, 2006; Forte & Radicella, 2002; McCaffrey & Jayachandran, 2019; Mushini et al., 2012; Wang et al., 2018). This issue is, however, not crucial for the purpose of our paper, that is, to use σ_ϕ as a proxy for the presence of density irregularities. Also, for completeness, spectrograms of the raw phase data are shown in the supporting material in Figure S4. Those may indeed provide further information about the scales of the irregularities involved and overcome issues related to the σ_ϕ index as suggested by van der Meeren et al. (2014, 2015). Furthermore, geometric enhancements of scintillations may occur when the signal path is parallel to the irregularity axis. At the onset of enhanced phase scintillations, the elevation angle of the satellites of interest ranged between around 32° to around 42°, roughly corresponding angles of about 40° to about 50° between the signal path and the magnetic field, which had local dip angles greater than 82° (calculated using International Geomagnetic Reference Field-12 (Thébault et al., 2015)). Thus, we do no expect this to be a critical issue for the purpose of this study.

We use the L1 frequency for scintillation and dual frequencies for TEC (L1 and L2Y for GPS, L1 and L2P for GLONASS). No Galileo satellite was tracked during the time of interest. For TEC, we calculate the vertical TEC (vTEC) (Alfonsi et al., 2011; Mannucci et al., 1993). The data have been scrutinized to filter out multipath effects using long-term observations for each station but we also apply a cutoff elevation angle of 25° for all receivers to minimize remaining errors. The GNSS ionospheric pierce points (IPPs) have been projected to 300 km altitude, which roughly corresponds to the peak electron density observed by the magnetic field-aligned fixed 42 m ESR dish (shown in Figure S3).

We use the fully steerable ESR 32-m antenna (Wannberg et al., 1997) for deriving 2D maps of densities, velocities, and temperatures. The scans were performed in azimuth at a fixed elevation angle of 30° , providing "fan plots" of the ionospheric plasma conditions with an integration time of 6.4 s (Carlson et al., 2002). In the rest of the paper, the abbreviation ESR always refers to the 32 m dish.

In addition, we use in situ measurements right above the ESR field of view. These were obtained by DMSP F17, which has an orbital period of about 101 min at around 840 km altitude (e.g., Kilcommons et al., 2017; Rich & Hairston, 1994). We use the Level 2 data obtained at a cadence of 1 s from the Special Sensors-Ions, Electrons, and Scintillation (SSIES) instruments and show ion density and velocity data from the Retarding Potential Analyzer (RPA) and from the Ion Drift Meter (IDM), respectively (Hairston, 2019; Rich, 1994b). Data with quality flags "poor" are removed. We also use the new DMSP database of precipitating electrons and ions obtained from the Special Sensor J (SSJ) 5 instrument (Redmon et al., 2017), which measures fluxes from 30 eV to 30 keV each second (Hardy et al., 2008).

Numerical models are also used in this study. The GEMINI model (Geospace Environment Model of Ion-Neutral Interactions) is a 3-dimensional (3D) multifluid-electrodynamic model of high latitude ionospheric plasma instabilities (Zettergren et al., 2015). GEMINI includes aeronomical, transport, and electrodynamic processes relevant to the formation of ionospheric fluid instabilities such as GDI and KHI (e.g., Deshpande & Zettergren, 2019). The model comprises a fluid system of equations (Blelly & Schunk, 1993; Schunk, 1977), describing dynamics of the ionospheric plasma, self-consistently coupled to an quasi-electrodynamic treatment of auroral and neutral dynamo currents (Zettergren et al., 2015). The fluid system is a set of three conservation equations (mass, momentum, and energy) for each ionospheric species s relevant to the E-, F-, and topside regions ($s = O^+, NO^+, N_2^+, O_2^+, N^+, H^+$). Terms in the conservation of mass equations encapsulate chemical production and impact ionization (via the method of Fang et al. (2008) or the GLOW energetic electron transport code of Solomon and Qian (2005) and chemical loss (taken from Diloy et al., 1996; St-Maurice & Laneville, 1998, and references therein), while photoionization sources are calculated according the method presented in Solomon and Qian (2005) using solar fluxes from the EUVAC model (Richards et al., 1994). GEMINI's momentum equations includes time-dependence and ion inertial effects relevant to plasma instabilities of interest, as well as pressure, gravity, electromagnetic, and collisional drag forces. Full ion and electron energy equations are also solved by GEMINI.

SIGMA is a 3D electromagnetic wave propagation model capable of simulating scattering, diffraction, wave refraction, and reflection through an arbitrary density field, including a turbulent plasma simulated by a physics-based model like GEMINI. SIGMA handles propagation of a radio frequency signal from a moving satellite to the ground through multiple phase screens (MPS) anywhere on the globe (Deshpande et al., 2014). The model is especially applicable at high latitudes, where the magnetic field inclination is changing with the location, making the geometry complicated. Inside SIGMA, first a spatial electron number density distribution from a spectral model for irregularities or the number density itself from a plasma model (such as GEMINI) translated into phase screens is inserted, and then the signal is propagated between the multiple phase screens and to the ground. SIGMA outputs 2D complex signal propagated to the ground as well as high-rate GPS scintillation phase and power time series with 50 Hz sampling frequency, from which S_4 and σ_ϕ can be easily extracted. High rate phase and power are detrended and filtered in order to eliminate any low-frequency effects including the satellite motion (Van Dierendonck et al., 1993).

For this paper, we simulate the time-dependent evolution (through both linear and nonlinear stages) of KHI with GEMINI and then use SIGMA to propagate GPS signal from satellite vehicle number PRN $G28$ through simulated KHI electron density irregularities at the time of interest; the methodology is an extension of that applied to study GDI in prior related work (Deshpande & Zettergren, 2019).

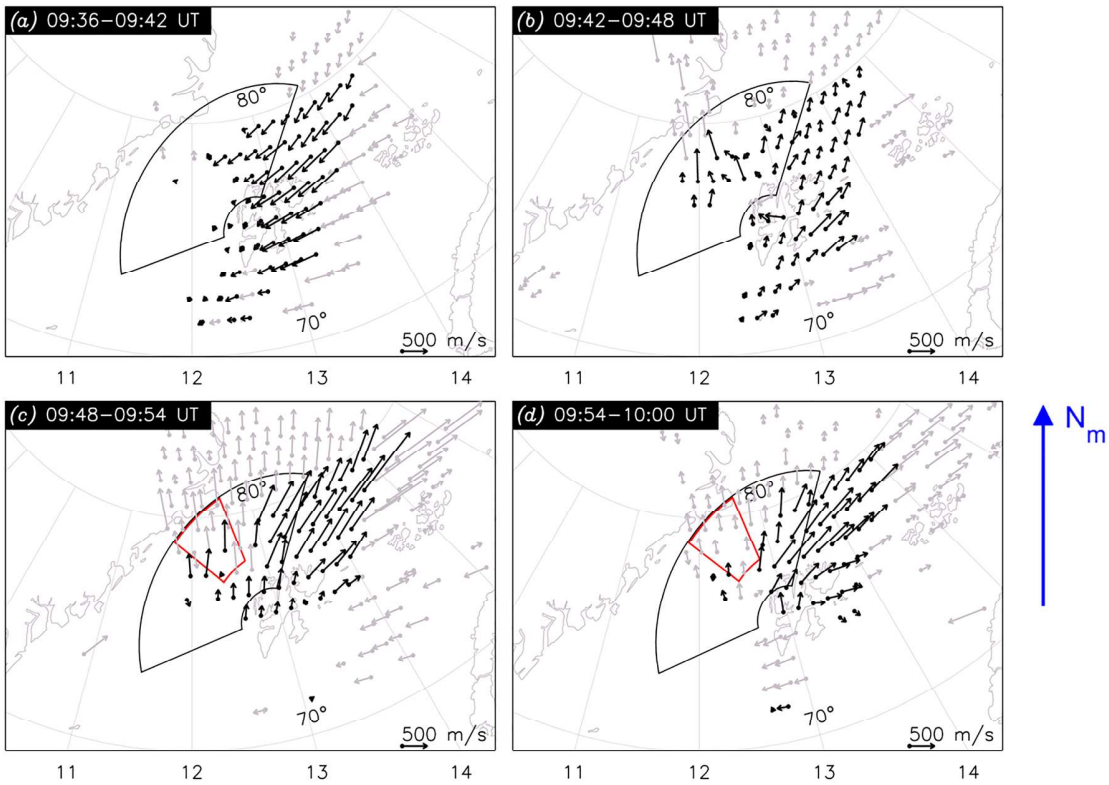

Figure 1. SuperDARN velocity vectors (black arrows) derived by combining data from the Hankasalmi and Pykkvibær radars and integrated over 6 min. The grey vectors show line-of-sight velocities from single radars where not enough data from both radars were available to produce 2D flow vectors. Coordinates are AACGM with MLTs shown on the bottom of each panel. North is roughly on the top of each panel, as illustrated by the blue arrow. The fan shape shows the ESR field of view and the red box highlights the region with largest phase scintillation indices.

3. Data Presentation

In this section, we present the observations from the different instruments described in Section 2. We first outline the large-scale context and then zoom into the meso- and smaller-scale observations.

3.1. Large-Scale Context

The solar wind conditions were relatively stable around the time of the event, that is, between about 09:37 UT and 10:00 UT on November 30, 2014. For completeness, a figure showing OMNI data is given in the additional material in Figure S1 and the main characteristics of the solar wind during the interval of interest are described below. The IMF B_x component was positive with values ranging between about 9 and 4 nT, while the IMF B_y component decreased from 0 to about −9 nT right after 09:40 UT. IMF B_y then remained quite stable around −9 nT. The IMF B_z component turned slightly negative at about 09:38 UT (with values close to −3 nT), remained negative for about 15 min, and increased to close to zero from about 09:52 UT. The solar wind velocity took values between about 375 and 395 km/s between about 09:37 UT and 10:00 UT, and the proton density ranged between six and nine particles per cubic meter.

In order to frame the large-scale ionospheric flow context above Svalbard during the time of the event, we use the Doppler drift velocity data from SuperDARN radars, shown in Figure 1. The coordinates are Altitude-Adjusted Corrected Geomagnetic Coordinates (AACGM) (Baker & Wing, 1989), with magnetic local time (MLT) shown on the bottom of each panel. Geomagnetic North (N_m) is roughly on the top of each panel, as illustrated by the blue arrow. The solid black line shows the ESR field of view, and the red box highlights the region with largest phase scintillation indices (presented in detail below). The black arrows illustrate the velocity vectors derived by combining data from the Hankasalmi and Pykkvibær radars, and the grey arrows show line-of-sight velocities from single radars, that is, when it was not possible to combine the data from the two radars.

During the time of the event, Svalbard was located postnoon at around 13 MLT, with the ESR field of view being located around 12 MLT. Between 09:36 UT and 09:42 UT, the large-scale plasma flow above and north of Svalbard was directed towards southwest, as seen in Figure 1a. This flow motion reversed completely between 09:42 UT and 09:48 UT, as shown in 1b: the large-scale plasma motion was now generally poleward. Between 09:48 UT and 09:54 UT, the poleward (northeast) flow displayed in 1c intensified significantly and, in the field of view of ESR, it reached values of about 1,000 m/s north of Svalbard. During the next 6 min, enhanced poleward plasma circulation remains visible in Figure 1d (this goes on until about 10:10 UT, not shown).

To frame the large-scale background density, Figures 2a1 to a4 display four GPS TEC maps around Svalbard using data from the Madrigal database (Rideout & Coster, 2006; Vierinen et al., 2016). Geographic north is on the top of each panel, and the blue arrow with label N_m shows the direction to geomagnetic North. For better visualization, each TEC map has been averaged using a median filtering process including the previous and the next GPS TEC maps (Thomas et al., 2013). In addition, each panel shows 5 min of phase scintillation indices σ_ϕ centered around the times shown in the top right corners. The phase scintillation index is displayed as dots for low phase scintillation ($\sigma_\phi < 0.25$ rad), medium circles for intermediate phase scintillation ($0.25 \leq \sigma_\phi < 0.5$ rad), and big circles for strong phase scintillation ($\sigma_\phi \geq 0.5$ rad). A few selected PRNs detected from the NYA receiver are highlighted using different colors, with the letter "R" standing for GLONASS and "G" for GPS. The fan-shaped line shows the ESR field of view.

As can be seen in Figure 2a1, the event began with the presence of a region of enhanced density poleward of Svalbard, hereafter referred to as "the density reservoir". This region is highlighted by the dotted oval. The enhanced solar EUV plasma density can be seen further south separated by a region with low density above Svalbard, that is, a trough. Comparing with SuperDARN data shown in Figure 1a, this corresponds to the time interval during which the flow reversed from approximately sunward to antisunward. In general, the phase scintillation level observed was low in the entire field of view. In Figure 2a2, the TEC map remains quite similar with a slight poleward motion of the high density reservoir. In this panel, enhanced phase scintillation indices appear between the large density at high latitudes and the trough. Values of $\sigma_\phi \geq 0.5$ rad persisted in the same region in Panels a3 and a4, during which a clear poleward motion of the high-density region can observed. This is consistent with the large-scale flow pattern observed by SuperDARN in Figure 1c,d. In the end, the electron density was low in the field of view of ESR, but σ_ϕ remained enhanced.

To better visualize the evolution of the GNSS measurements, Figure 2b–m shows the time series for selected PRNs detected from NYA. *G*11 was chosen to illustrate observations at lower latitudes in the trough while *R*12, *R*22, and *G*28 were initially close to the boundary between the trough and the density reservoir and detected the strongest phase scintillation indices. *R*13 is also shown as it detected enhanced phase scintillation indices at higher latitudes. Panels b to d show vTEC with respect to time. In Panel b, vTEC takes values below about 10 TECU, consistent with the density trough observed in the TEC maps. In Panels c and d, vTEC is relatively constant until about 09:48-09:49 UT, after which it decreases. At the end of the interval, the vTEC values observed from NYA in the northern portion of the ESR are similar to vTEC in the trough, consistent with Panel a4. In Panels b to d, vTEC also becomes relatively more irregular with time. This can be better seen by looking at the absolute value of the ROT shown in Panels e to g: |ROT| is larger from the middle of the interval. A maximum of 4 TECU/min is reached at 09:50 UT for *R*22 and *R*12 in Panel f and at 09:51 UT for *R*13 in Panel g.

Figure 2h–j shows the amplitude scintillation index S_4 with respect to time. The values remain low with some small increases in Panel j and k.

Panels k to m display the phase scintillation index σ_ϕ with respect to time. In the density trough, $\sigma_\phi < 0.2$ rad during the entire time interval, as can be seen in Panel l. The onset of large phase scintillation index is detected by PRNs *R*12, *R*22, and *G*28 at 09:49 UT while PRN *R*13 sees a maximum in σ_ϕ about 3 min later. The enhanced values of σ_ϕ are not observed in the regions with largest vTEC, but coincide with the decrease in vTEC observed in Panel c and d.

3.2. Meso- and Small-Scale Observations

Now that the large-scale framework has been presented, insights into the meso-scale configuration can be obtained from ESR. Figure 3 shows four ESR fan plots labelled with S_0 to S_3 in geographic coordinates. For

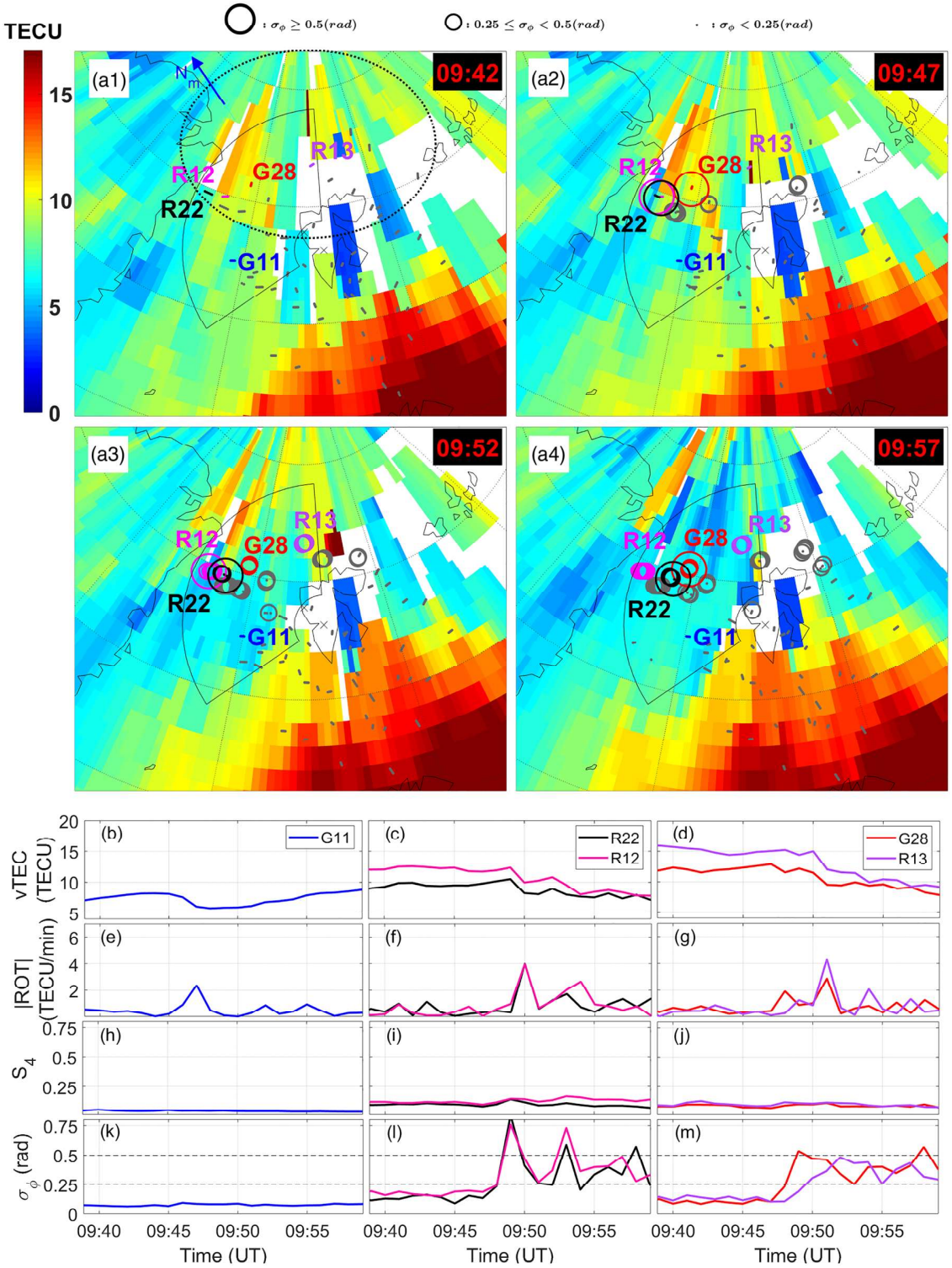

Figure 2. a1 to a4) GPS TEC maps for four time intervals of 5 min using data from the Madrigal database with phase scintillation indices obtained from four receivers on Svalbard overlaid. The phase scintillation level is displayed as black dots for low scintillations ($\sigma_\phi < 0.25$ rad), medium circles for intermediate scintillations ($0.25 \leq \sigma_\phi < 0.5$ rad), and big circles for strong scintillations ($\sigma_\phi \geq 0.5$). The colored numbers highlight selected PRNs tracked from the receiver at Ny-Ålesund. The letter "R" stands for GLONASS and "G" for GPS. The fan-shaped solid line shows the ESR field of view while the dotted oval in a1) highlights the density reservoir. Panels b to m show the time series of vTEC (b,c,d), $|ROT|$ (e,f,g), S_4 (h,i,j), and the phase scintillation index σ_ϕ (k,l,m) for the selected PRNs between 09:37 UT and 10:00 UT.

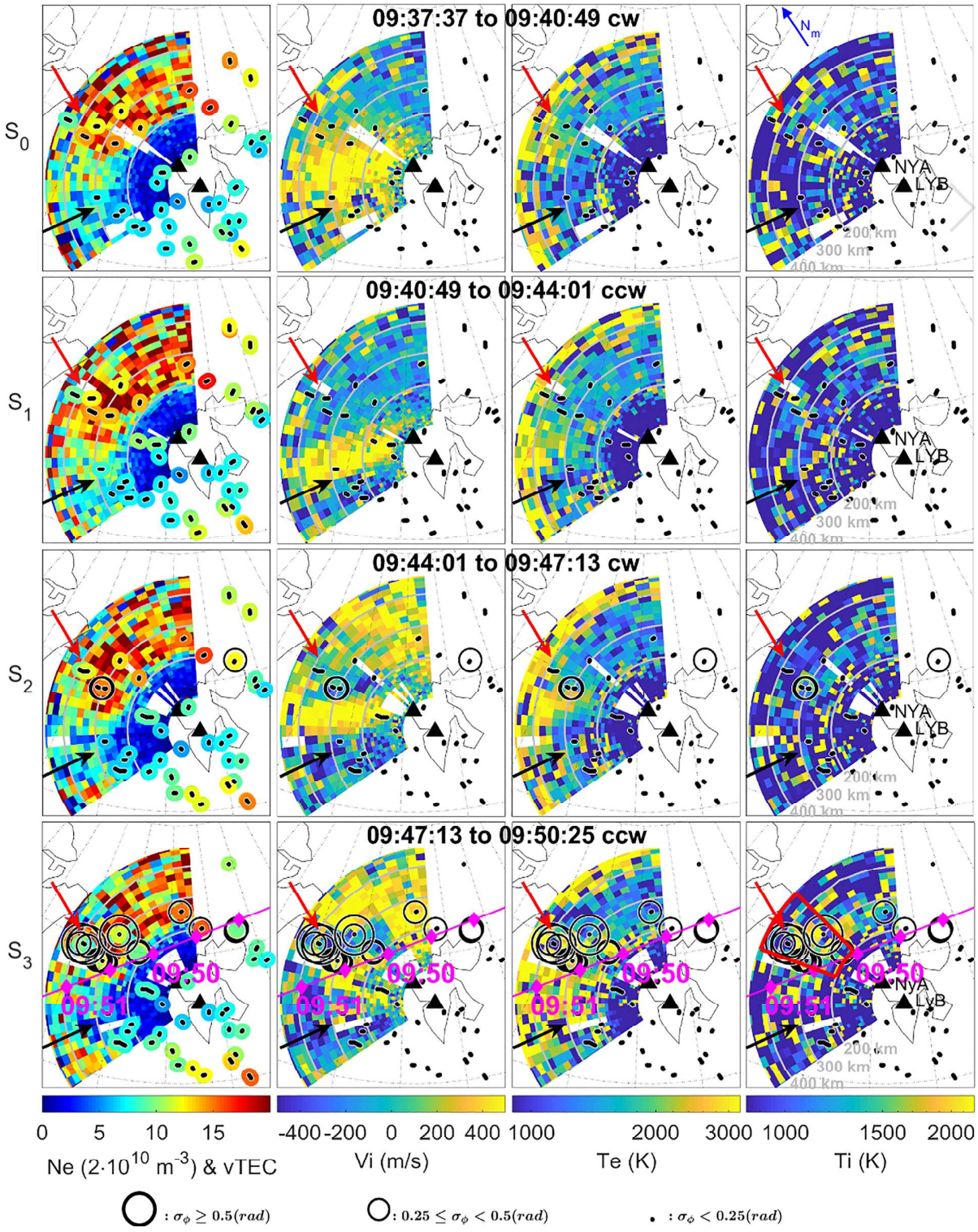

Figure 3. Each row (labelled with S_0 to S_3) is an ESR fan plot with the corresponding scanning time shown in black in the center. "cw" and "ccw" stand for clockwise scan and counter-clockwise scan, respectively. Left column: ESR density and GNSS vTEC. Second column: ESR line-of-sight ion velocity v_i. Third column: ESR electron temperature T_e. Fourth column: ESR ion temperature T_i. The black dots and circles illustrate different phase scintillation levels. The magenta line and times (in UT) in the bottom row illustrate the orbit of DMSP F17. The red and black arrows highlight regions of interest and the red box is the same as the one in Figure 1.

visualization purpose and comparison with SuperDARN, a blue arrow points towards geomagnetic north (N_m), and the same red box as in Figure 1 is shown in the last panel. Each row corresponds to one scan covering 120° in azimuth in 192 s. The GNSS data from all four receivers are superimposed on the ESR scans. The GNSS vTEC is color-coded, while the phase scintillation level is displayed as black dots for low phase scintillation ($\sigma_\phi < 0.25$ rad), medium circles for intermediate phase scintillation ($0.25 \leq \sigma_\phi < 0.5$ rad), and big circles for strong phase scintillation ($\sigma_\phi \geq 0.5$ rad). The first column shows the electron density (N_e) measured by ESR with vTEC. The second column shows ESR line-of-sight ion velocity v_i and σ_ϕ. The third and fourth columns show σ_ϕ with the ESR electron temperature (T_e) and the ESR ion temperature (T_i), respectively. The altitudes (200, 300, and 400 km) of the ESR beams are also displayed as grey lines. Note that the data above 400 km in regions with low density is quite uncertain (with errors that can be larger than 50% in some bins). It is, however, kept here to show the full ESR scan beams. For visualization purpose, the PRNs are not repeated, but the red arrow points toward PRNs $R22$, $R12$, and $G28$, while the black arrow towards $G11$. The time history of the event shown in Figure 3 is presented in detail in the following:

In the first scan shown here, S_0 (from 09:37:37 UT to 09:40:49 UT), a reservoir of high density can be observed poleward of Svalbard above 200 km altitude (red and orange region in ESR Ne and vTEC in the top left panel, highlighted by the red arrow), equatorward of which a trough of low density can be observed (blue region in ESR Ne and vTEC, highlighted by the black arrow). At F-region altitudes, densities take representative values of $4 \cdot 10^{11}\ m^{-3}$ and $1.5 \cdot 10^{11}\ m^{-3}$ in the reservoir and trough, respectively. A broad region of westward flow with median velocities reaching about 700 m/s (yellow, away from the radar) can be seen above Svalbard, that is, in the trough region, and directed towards the radar at higher latitudes (blue, towards the radar) with velocities of about −100 m/s. This is generally consistent with the SuperDARN velocities shown in Figure 1a, exhibiting a southwest flow. No significant enhancements in the electron and ion temperatures can be observed. During that time interval, the phase scintillation level is low.

In the next scan, S_1 (from 09:40:49 UT to 09:44:01 UT), the trough and higher density reservoir are still present, in agreement with the TEC map shown in Figure 2a1. No significant enhancements in ESR T_e and T_i can be observed. In the velocity scan, the broad region of westward flow has turned into a narrower flow channel (yellow) with velocities reaching values of about 600–800 m/s. The flow outside of this channel is generally in the opposite direction (blue) with median velocities between about 200 and 350 km altitude of about −150 to −200 m/s. The equatorward side of the flow channel is located in the density trough and the poleward side near the boundary between the trough and the higher density northward. The phase scintillation level is still low.

In the next scan, S_2 (09:44:01 UT to 09:47:13 UT), the density trough and reservoir are still similar. The flow channel has moved slightly poleward and exhibits velocities reaching 900 m/s, while the plasma motion towards the radar (blue) on its flanks reach values of about −500 m/s. This implies maximum velocity differences $\Delta V \approx 1400$ m/s. In addition, a (geographic) poleward flow of about 500 m/s north of Svalbard is now visible, in accordance with the large-scale convection pattern seen by SuperDARN in Figure 1b and the GPS TEC map in Figure 2a2. A new feature in this scan is the appearance of a thin East-West channel of enhanced T_e between 300 and 400 km, collocated with the poleward side of the flow channel. Low-energy cusp particle precipitation will result in enhanced T_e in the cusp ionosphere (Vontrat-Reberac et al., 2001), which is often seen in connection with auroral arcs (Doe et al., 2001; Valladares & Carlson, 1991; Weber et al., 1989). The channel of enhanced T_e in Figure 3 S_2 is therefore interpreted as a signature of active cusp precipitation and auroral emissions. The conditions are sill relatively quiet, with a low scintillation level in general. In the ESR field of view, an increase of the phase scintillation index (to $0.25 \leq \sigma_\phi < 0.5$ rad) can, however, be observed at the poleward boundary of the flow channel, that is, close to sheared-flow, and near the region of enhanced T_e. This is also located in the high-density reservoir (close to the red arrow) near the boundary between the low- and high-density regions and in the shear region. On the other hand, there are still no significant increases in the phase scintillation indices on the equatorward side of the RFE in the trough (highlighted with the black arrow).

During the next scan, S_3 (from 09:47:13 UT to 09:50:25 UT, that is, after about 10 to 13 min since S_0), the trough and high-density reservoir are still present. The flow channel has moved slightly poleward since S_2 and is less uniform, but with similar velocity magnitudes (slightly larger). The reversed flow poleward of the flow channel matches the definition of an RFE (Rinne et al., 2007). The poleward motion north of Svalbard is also still present, consistent with SuperDARN and TEC maps Figures 1c and 2a2. The channel of enhanced

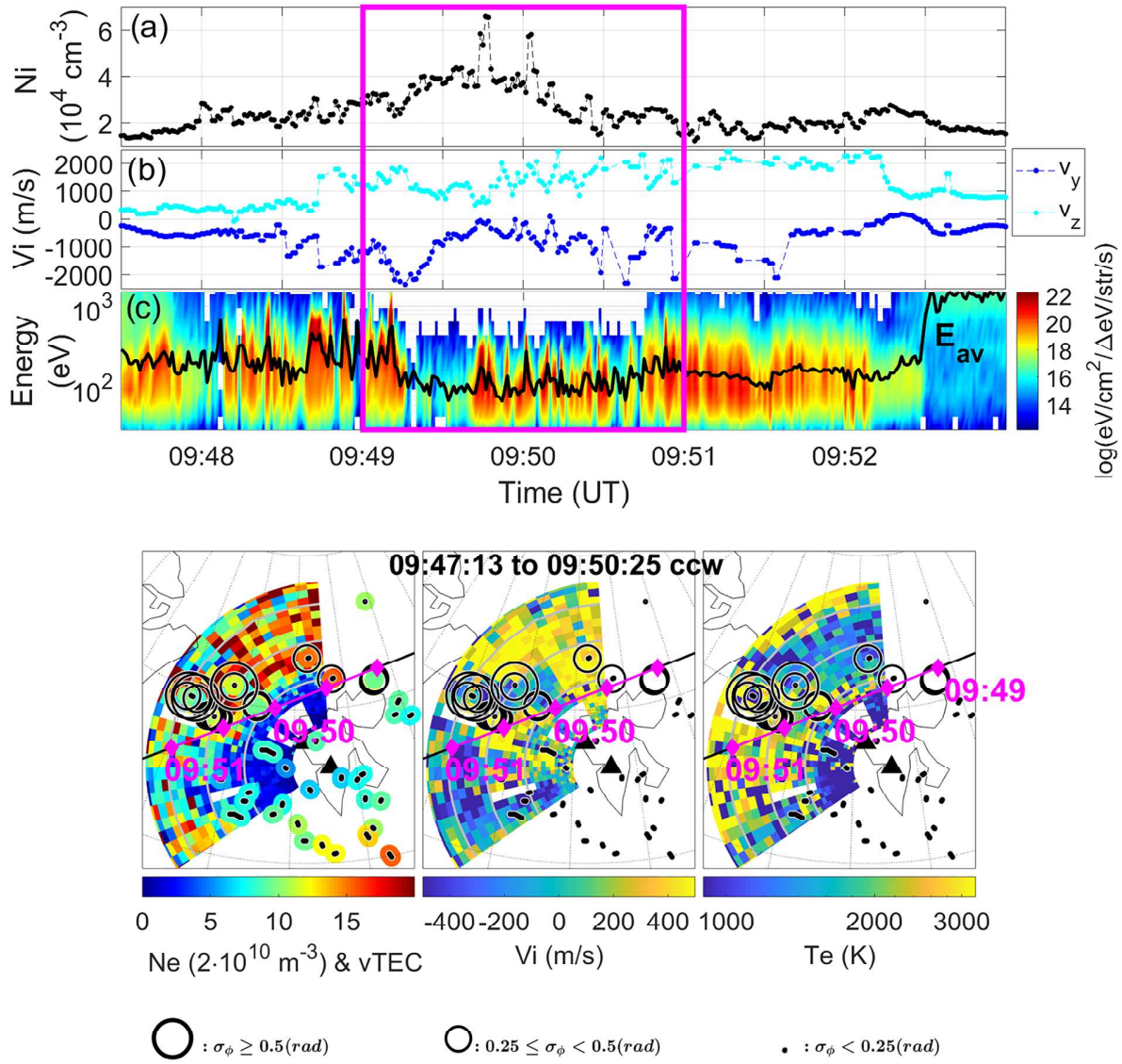

Figure 4. (a) Ion density measured on-board DMSP F17. (b) Horizontal cross-track velocity (v_y, dark blue) and upward cross-track velocity (v_z, cyan) obtained from DMSP F17. (c) Electron particle precipitation spectrum (color-coded) and average energy E_{av} (black line) measured by DMSP F17. The magenta box illustrate the time interval during which DMSP F17 flew over the Svalbard region. In the bottom part of the figure, the ESR scan at the time of conjunction between the radar and DMSP is shown. This corresponds to scan S_3 Figure 3. The magenta part of the orbit corresponds to the time range of the magenta box.

T_e has now expanded equatorward into a broad region above 180–200 km altitude. This may indicate the presence of broader region of cusp particle precipitation. The poleward region of this enhancement in T_e matches the RFE region (blue v_i), and the equatorward part extends to the middle of the trough. At this stage, enhancements in T_i to about 2,500 K also appear above about 200 km altitude. During this scan, enhanced phase scintillation indices are detected in the RFE on the poleward side of the flow channel and of the region with enhanced T_e. This is also collocated with the area exhibiting ion heating. On the other hand, no significant scintillations are observed in the density trough on the equatorward side of the flow channel (black arrow).

During scan S_3, DMSP F17 orbits above the field of view of ESR between about 09:49 UT and about 09:51 UT, as indicated by the magenta line. The observations made by DMSP F17 are shown in Figure 4a-c, with a magenta box highlighting the interval during which DMSP orbits above the region of interest. For visualization purposes, scan S_3 is also shown (only N_e, v_i and T_e) with the magenta part of the trajectory corresponding

to the magenta box. Figure 4a depicts the ion density, which is quite irregular. One larger peak with steep gradients can be seen at about 09:49:30 UT and one at 09:50:00 UT.

Panel b shows two components of the ion velocity measured on-board DMSP F17: the horizontal cross-track component (dark blue, v_y) with negative sign being approximately antisunward, and the upward component (cyan, v_z). Both components are highly inhomogeneous with several intervals of fast flows ($\geq$ 2,000 m/s) and several gradients in the region of interest. In particular, a flow channel with a maximum of $-2,921$ m/s reached at 09:50:36 UT can be observed. This is collocated with the location of the flow channel, as can be seen in the ESR v_i scan (yellow, away from the radar).

Figure 4c shows the electron precipitation differential energy flux (color coded), with the average energy (E_{av}) displayed as a black line. From about 09:49:45 UT to about 09:52:00 UT, the average energy of precipitating electrons ranges between about 100 and 300 eV. This roughly corresponds to the time interval during which DMSP orbits above the region of enhanced ESR T_e, supporting that it is due to low-energy "soft" particle precipitation (Doe et al., 2001; Valladares & Carlson, 1991; Vontrat-Reberac et al., 2001; Weber et al., 1989). In this interval, electron precipitation is finely structured into short bursts with typical lengths of 1 to 2 s (corresponding to $\sim$ 8–16 km). This is especially pronounced between 09:49:45 UT and 09:51:00 UT. This interval matches the poleward region of enhanced T_e observed above 180-200 km altitude in the ESR scans. Noteworthy is also the coincidence between the two largest electron fluxes in the interval of interest and the density enhancements previously mentioned at 09:49:45 UT and 09:51:00 UT (compared with Figure 4a).

As presented in Figure 2, the conditions remained perturbed after the onset of enhanced phase scintillations around 09:49 UT. According to the three next ESR scans (shown in Figure S2 in the supporting information), enhanced phase scintillation indices persist during the next ten minutes in the vicinity of fast ($|v_i| > 1000$ m/s) inhomogeneous flows, enhanced T_e, and T_i, and where the observed density has significantly decreased, that is, consistent with the poleward flow motion observed by SuperDARN and the TEC maps shown in Figure 2a3,a4. It is worth mentioning that no scintillations were observed on the equatorward part of the trough (on the boundary with the low latitude solar EUV).

To further highlight the presence of small-scale plasma density structures, Figure 5 shows the spectral widths obtained from SuperDARN, which provide backscatter from decameter-scale irregularities (Chisham et al., 2007). The times and the layout are similar to ones shown in Figure 1, that is, geomagnetic North (N_m) is on top, the red box illustrates the region with strongest phase scintillation, and the black line the ESR field-of-view. In the beginning of the event, that is, before the flow channel, the spectral width is low in the ESR field-of-view, as can be seen in Figure 5a. In Panel b, which corresponds to the time interval during which the convection reversed and the narrow channel appeared, an increase in the spectral width can be observed in the middle and northern part of the of the ESR field of view. Figure 5c shows the spectral width for the time interval including the onset and largest phase scintillation levels. Large values of spectral width (225 m/s) are seen to coincide with the region of strongest scintillation, as highlighted by the red box. In Panel d, the spectral width decreases in the ESR field-of-view but is still enhanced compared to the beginning of the event (Panel a)).

Before discussing the observations, we briefly summarize the observations leading to enhanced phase scintillations. The event started with a preexisting southward-moving broad region of enhanced density poleward of a density trough, with representative values of about $4 \cdot 10^{11}\ m^{-3}$ and $1\text{-}2 \cdot 10^{11}\ m^{-3}$, respectively (Figures 2 and 3 scans S_0-S_1). The large-scale flow reversed and a mesoscale channel of enhanced convection near the boundary between the high- and low-density plasmas appeared with median velocities reaching 700–900 m/s inside and about -100 to -500 m/s outside of the channel (Figures 1 and 3 scans S_1-S_3). This implies maximum total velocity differences between the flow channel and its surrounding reaching about $\Delta V \approx 1,400$ m/s (over several radar beams). It is worth mentioning that DMSP observed even higher velocities in the flow channel. Furthermore, enhanced T_e likely due to fine-structured low-energy particle precipitation and a broader poleward motion of about 500 m/s are then visible in Scan S_2.

4. Discussion of the Observations

At high latitudes, enhanced density irregularities and large phase scintillations generally peak in the cusp and in the auroral oval, regions known to be ionospheric footprints of the coupling between the solar wind and magnetosphere (Jin et al., 2015, 2019; Prikryl et al., 2015). Inhomogeneous flows being common features

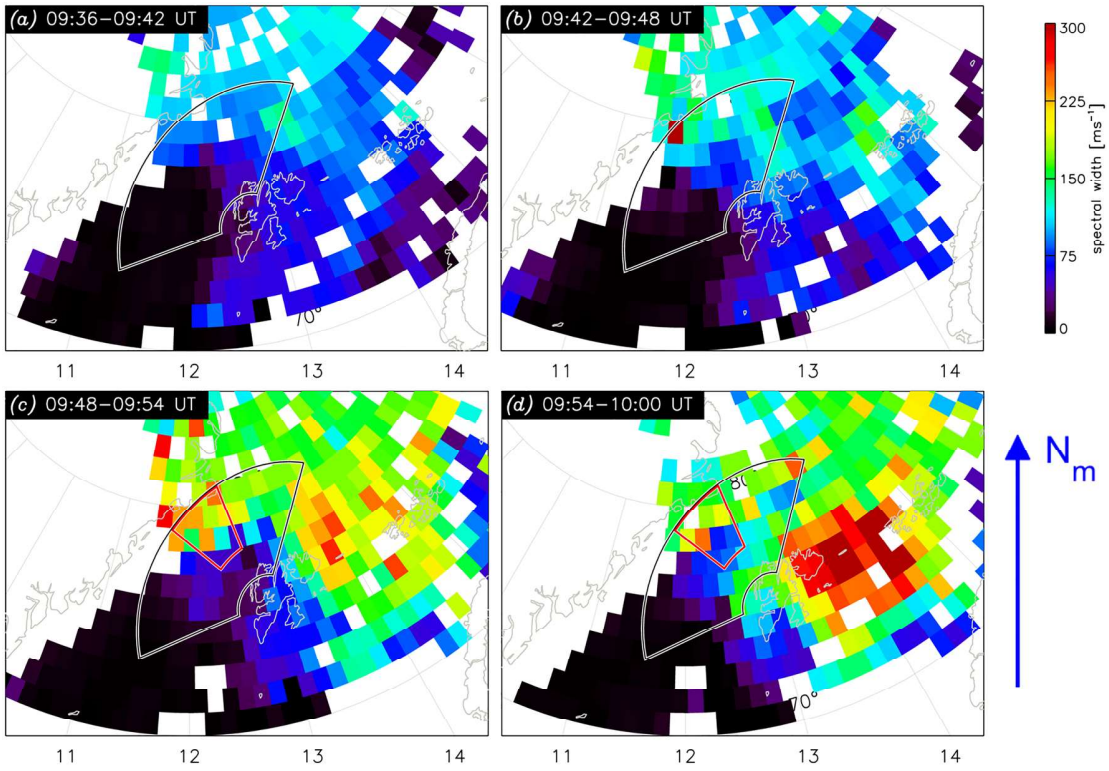

Figure 5. SuperDARN spectral width derived by combining data from the Hankasalmi and Pykkvibaer radars on a grid and integrated over 6 min. Coordinates are AACGM with MLTs shown on the bottom of each panel. The fan shape illustrates the ESR field of view and the red box the region with largest phase scintillation indices.

due to this coupling (e.g., Basu et al., 1994; Clauer, 2003; Heppner et al., 1993; Oksavik et al., 2004b; Pinnock et al., 1993; Rinne et al., 2007; Southwood, 1987), we investigated the concurrence of enhanced scintillation indices and a narrow channel of intensified convection with flow shears on its flanks including an RFE. Previous studies noted the presence of small-scales plasma irregularities (e.g., Oksavik et al., 2011; Spicher et al., 2016), moderate phase scintillation ($\sigma_\phi < 0.3$ rad) and low-amplitude scintillation (Jin et al., 2017, 2019b) in relation to RFEs. Here, we present an evidence that strong phase scintillation indices ($\sigma_\phi > 0.5$ rad) can arise from such events.

The event started with a preexisting broad region of enhanced density at high latitudes poleward of a density trough, a scenario different to the more typical case related to polar cap patch formation from the low latitude solar EUV plasma (e.g., Carlson, 2012; Jin et al., 2017, end references therein) or directly from auroral precipitation (Oksavik et al., 2006). The strongest phase scintillation and enhanced spectral width observed within the field of view of ESR arose shortly after a reconfiguration of the ionospheric convection on the poleward side of a narrow cusp flow channel, supporting that magnetosphere–ionosphere coupling is an important element in the generation of small-scale plasma irregularities and scintillation in the cusp (e.g., Jin et al., 2017; Prikryl et al., 2015). The onset of enhanced scintillations coincided with the presence of sheared (reversed) plasma flows and fine-structured, low-energy particle precipitation at the boundary between the high-density reservoir and the low-density trough. No enhanced scintillation indices were detected on the equatorward side of the flow channel in the trough, even though fast sheared flows (with values as high as on the poleward side) and large T_e were apparent in that low-density region. Having preexisting high density such as the high-latitude plasma reservoir in our case appears thus to be a crucial component for the onset of enhanced scintillation. One plausible explanation for the higher scintillation level we observe compared to one associated with the RFE in Jin et al. (2019b) could indeed be related to the presence of the high-density region in our case. The latter RFE was characterized by conditions (flow shears, temperatures, densities, and vTEC) fairly similar to the ones we measure in our trough. Our observations reinforce the suggestions from Jin et al. (2015, 2017) that the combination of high density regions (polar cap patches in their case) and auroral dynamics create stronger scintillations than only auroral dynamics.

Recent modelling work was performed to study the effect of GDI on navigation signals (Deshpande & Zettergren, 2019), and here, as we observe inhomogeneous flows near the boundary between a density reservoir and a trough, we focus essentially on the KHI as a primary mechanism. We perform numerical simulations of the KHI and investigate in more detail the plausibility for it to generate density irregularities and associated phase scintillations in the cusp ionosphere.

5. Numerical Simulations

In the following, we present a quantitative, nonlinear analysis of KHI using numerical simulations from GEMINI-SIGMA. We use typical winter conditions and an initial configuration similar to the one leading to the strongest phase variations observed, that is, high- and low-density plasma regions separated by a flow shear, as shown in Figure 3 scans S_2 and S_3. These simulations are computationally expensive (taking several days with hundreds of processors), so we take the approach of running the simulation with representative values for our event rather than running through all reasonable combinations of input parameters. This modeling effort is, thus, not a parametric study but more of a demonstration of the feasibility of KHI as an agent to produce scintillation under similar situations.

The initial conditions needed to set up the KHI scenario, starting from an equilibrium ionosphere, are discussed in detail in Keskinen et al. (1988). This equilibrium prescribes definite relations between the velocity and density fields, such that initial Pedersen current divergences are zero. Here, we use initial conditions emphasizing the anticorrelation between high-density and high flow regions seen in the ESR scan which take the form as follows:

$$n_e(x, y, z, t_0) = n_{e0}(z) + n_{e1}(z)\left[\frac{1}{2} + \frac{1}{2}\tanh\left(\frac{y}{\ell}\right)\right] \tag{1}$$

$$v_x(x, y, z, t_0) = v_0 + v_1\left[\frac{1}{2} - \frac{1}{2}\tanh\left(\frac{y}{\ell}\right)\right], \tag{2}$$

where v_0 and v_1 are the flow values perpendicular to the magnetic field on each side of the shear, n_{e0} is the background density, n_{e1} is the maximum density, and ℓ corresponds to the scale size of the initial shear. It is not completely possible to constrain the scale size ℓ in the model as none of the measurements resolve the scales necessary to capture the fastest growing modes (e.g., DMSP samples are at 1 s, implying about 8-km resolution, ESR resolution is considerably larger). Thus, for this modeling study, we choose a somewhat arbitrary scale length $\ell = 1$ km on the initial density and shear to emphasize the plausible situation where irregularities develop in a time frame similar to what is observed, while we use values consistent with the ESR observations to constrain the flow and density values. The drift velocities are taken to be $v_0 \approx 0.1$ km/s and $v_1 \approx 1.2$ km/s, and the density parameters $n_{e0} = 1 \cdot 10^{11}$ m^{-3} and $n_{e1} = 4.5 \cdot 10^{11}$ m^{-3}. A small amount of additive noise is included in the initial conditions in order to seed the instability.

The development of KHI in the ionosphere depends on a number of parameters, including (a) inertial capacitance to conductance ratio, (b) Hall conductance, (c) background velocity and shear, (d) background density and density jump, and (e) shear transition scale length. As discussed in detail in Keskinen et al. (1988), the inertial capacitance to conductance ratio determines, to a degree, the growth rates of KHI and the general behavior of the instability in the nonlinear regime. KHI is triggered by polarization currents in the ionosphere-magnetosphere system and can be damped by a nonzero Pedersen conductance, which shorting of the instability through conduction currents flowing in the F-region. Pedersen effects also cause the nonlinear stages of the instability to progress differently, generally leading to more wave breaking and somewhat different spectrum of irregularities (Keskinen et al., 1988). It is not possible to completely cover this parameter space for the present study due to the time cost of running our models; hence, we fix the transition scale length at 1 km and perform two simulations having different values for inertial capacitance. The maximum Pedersen conductance over the grid for each run is $\sim$ 1.2 S, and the maximum inertial capacitances used in the simulations are $\sim$ 10 F (Case B) and $\sim$ 30 F (Case C). These values are within typical ranges cited in limited available KHI modeling literature (Huba et al., 1988; Keskinen et al., 1988).

Modeled evolution of KHI from GEMINI (Zettergren et al., 2015) is shown in Figure 6 at five different times illustrating the development of the irregularities for the Case B simulation (10 F inertial capacitance). The panels of this figure show density at 300 km altitude versus eastward and northward distance. A movie showing the entire simulated density in all three dimensions is given in the supporting material for this article (Movie S1). Figure 6a shows the model density following 220 s of evolution—the high-density reservoir

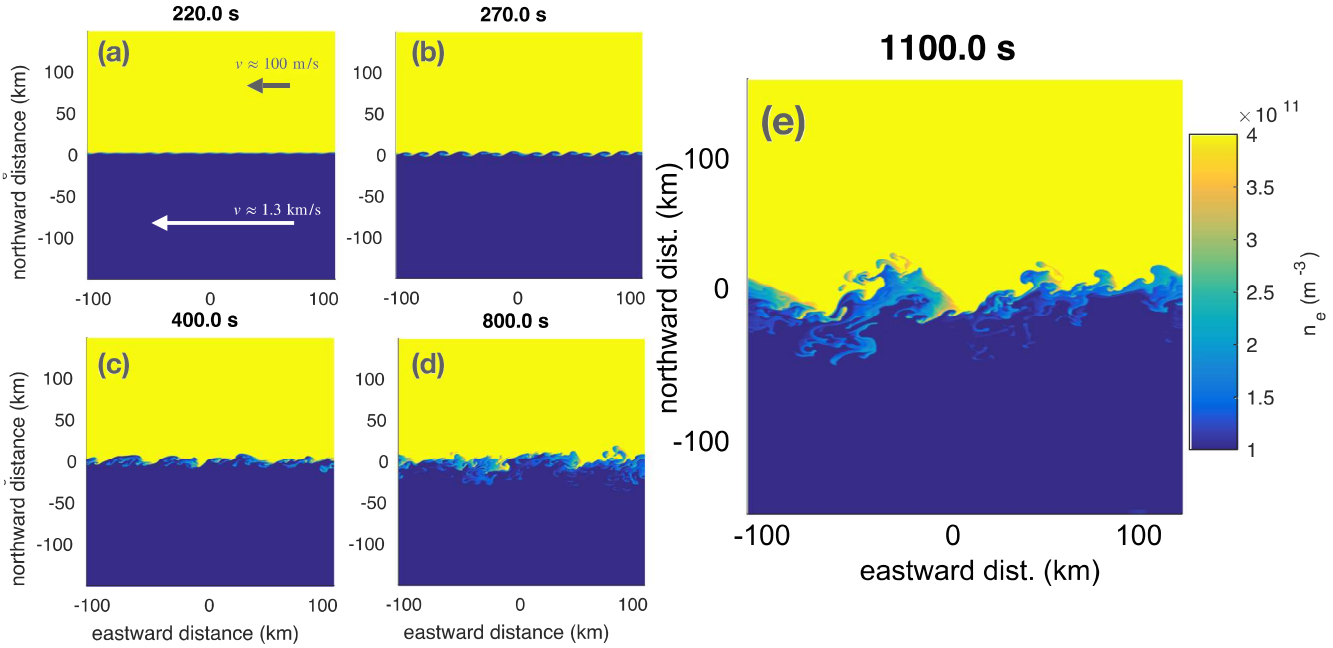

Figure 6. Snapshots from simulations Case B showing the electron density from GEMINI at 300 km altitude at different times during the development of the simulated Kelvin-Helmholtz instability.

and the low-density region are shown in yellow and blue, respectively. Barely visible waves seem growing in the boundary layer; otherwise, the simulated conditions are representative of the initially imposed state (from Figure 3). After about 270 s into the simulation, vortices characteristic of KHI have formed in the boundary layer; by 400 s, these vortices have begun to merge, while Pedersen current effects, manifesting as the appearance of breaking waves, are clearly present (c.f. Keskinen et al., 1988). Later stage evolution of the instability that we have simulated shows a rich spectrum of irregularity features (Panels d and e), including smaller-scale irregularities of the type that would be expected to impact ionospheric radio propagation. These turbulent features exhibit strong evidence of secondary instability. This includes apparently partially formed secondary vortices growing on the primary instability (these also tend to break, likely due to Pedersen effects) and also some suggestion of secondary GDI (e.g., distorted bubble-like regions of sharp discontinuity in density in Panel e).

Figure 7 shows the same initial condition but run with an inertial capacitance of 30 F (Case C). As compared to Case B, this run exhibits more vortex merging (Panel c), and larger vortices in the nonlinear stage (panel e), along with what appears to be bubble-like features (Panel e) reminiscent of secondary GDI. The three dimensional movie is also given in Movie S2.

The numerical simulations presented in Figures 6 and 7 show that density structures can be created relatively fast (∼ minutes) through the KHI using a shear scale length of $\ell = 1$ km. This time range is well contained within the time interval during which ESR observed the sheared flow (Figure 3 scans S_1 to S_3), making KHI a plausible primary candidate for the creation of the perturbations observed. It is also worth noting that the initial densities used for the simulations are smooth. Density structures may appear even faster for a realistic case where the density is not uniform to start with. On the other hand, increasing the scale length of the velocity gradient will generally increase the growth time and increase the wavelength of the fastest growing mode.

We then propagate GPS L1 signal through the ionospheric structures obtained from GEMINI using the SIGMA model (Deshpande & Zettergren, 2019; Deshpande et al., 2014). Estimating a precise KHI onset time is not straightforward, but our observations suggest that enhanced phase scintillations appear within about 3–6 min after the beginning of the flow channel event, maximize around 6–10 min, and last for about 20 min. Thus, we performed the analysis on three intervals of about 60 to 120 s long at different stages of the development of KHI. We did our simulations at 3, 9, and 16 min into the KHI development for GEMINI runs

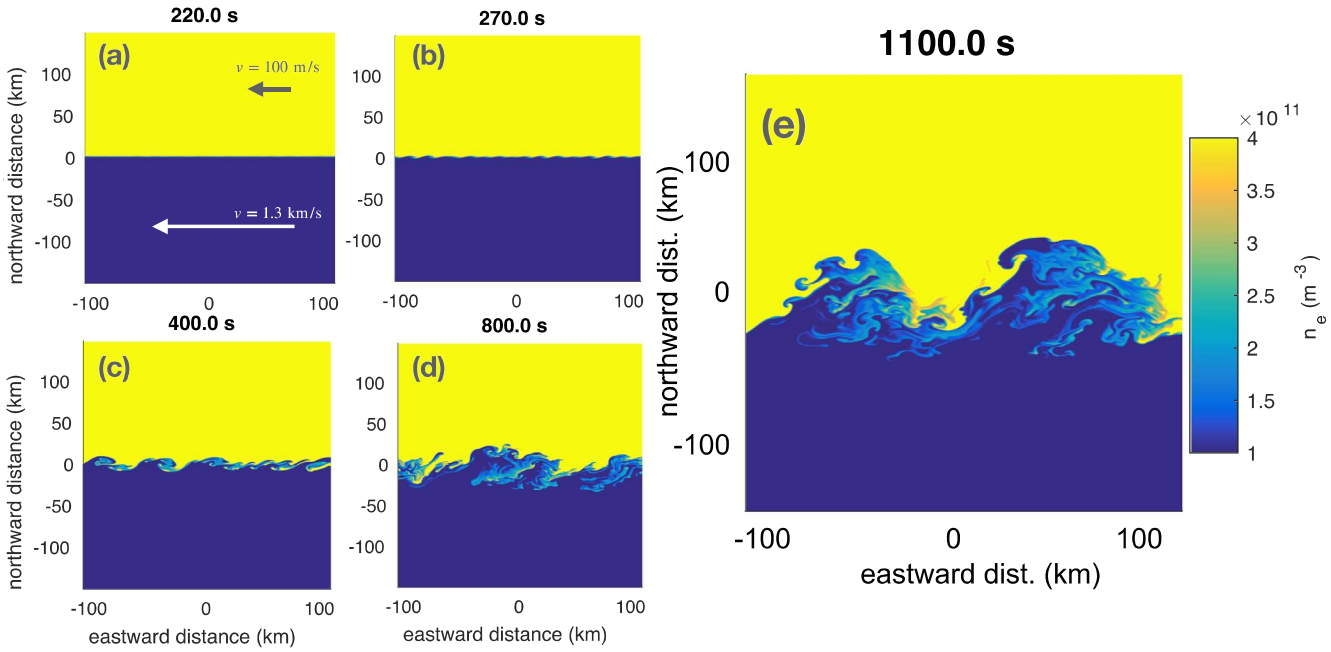

Figure 7. Snapshots from simulation Case C showing the electron density from GEMINI at 300 km altitude at different times during the development of the simulated Kelvin-Helmholtz instability.

(Cases B and C). As expected at high latitudes and consistent with our observations, our simulations yielded phase scintillations predominantly. Figure 8 shows 2D snapshots from the GEMINI (Case B) KHI movie of electron number density as the KHI evolves and their respective 2D propagated phases on ground through SIGMA (Case C is shown in Figure S5). Note that the high-density plasma exists on the poleward (northern) side. Detrended phase time series at the bottom panel of the figure is derived from the phase values taken at the receiver's location depicted by red crosses in Figure 8.

Notable phase variations can be observed in the middle and late stage of the simulations for Cases B and C, respectively, suggesting it to be slower than expected from the observations.

We also noticed in our simulations that the scintillations are stronger when either the ray path goes through the "steep" density gradients of the vortices (or simply the boundary between large density and low density in the beginning). We appear to have more small-scale structures riding on the density gradients or both. For example, phase scintillations tend to strengthen when larger vortices appear to enter or exit through the ray path for the GNSS signal at 990 and 1,035 s. Scintillations weaken when the ray path is in the middle of the larger vortices or earlier in the development of the instability without much smaller scale structures developed. The phase variations obtained from SIGMA reach maxima of about ±0.4 rad in Cases B and C, which is about one third of the maxima obtained from the real GPS data (see additional material Figure S4 *G*28). We have seen that high flow velocities contribute to faster, stronger, and more frequent scintillations (initial results from a case with faster flows, not shown and left for future work).

We envisage several possibilities to explain the difference between the model and observations. This includes (a) the contribution from other mechanisms (e.g., we do not attempt to model the precipitation), (b) underestimates of the flow values used in the model (DMSP observes much faster velocities than the field-of-view ESR ones, and initial simulations results with faster velocity of about 2 km/s increase the scintillation levels), (c) insufficient consideration of velocity filter effects (e.g., Wang et al., 2018), (d) difficulties to constrain the model to simulate the exact event (e.g., the use of smooth initial conditions, uncertainties related to the scale length of the shear, and the magnetospheric influence part, which is encapsulated in the inertial capacitance), and (e) limited resources to perform an inverse analysis to find the best fit of the GEMINI-SIGMA model output to the observations. This is because combined runs of over a thousand times would be expected for such an analysis and just one such run takes few days if not a few weeks on a high end computer.

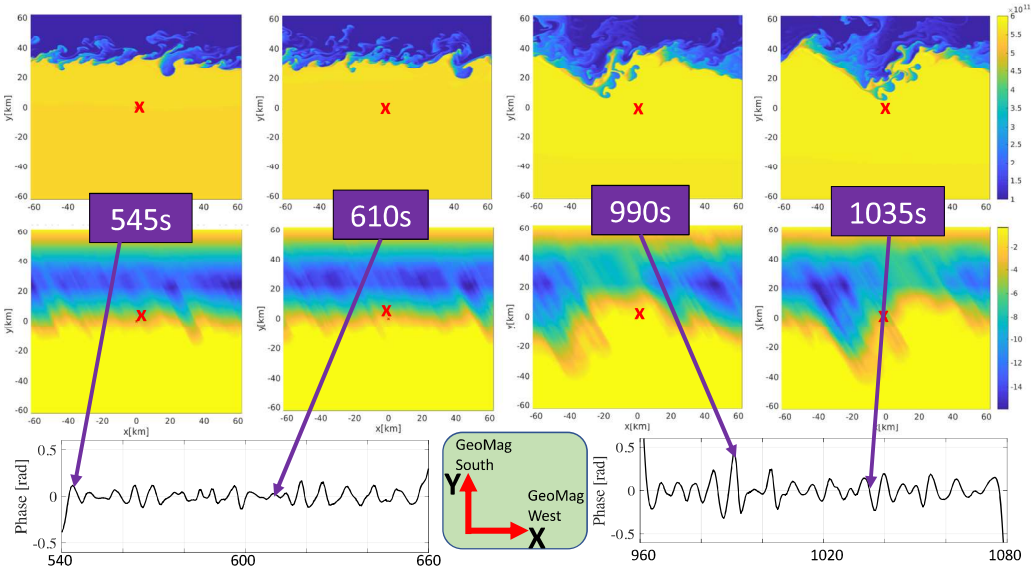

Figure 8. Snapshots from a SIGMA simulation depicting (top row) the 2D number density from GEMINI run Case B at the height of maximum F2, (middle row) the 2D phase in radians projected on the ground through SIGMA, and (bottom row), the resulting SIGMA phase time series showing scintillation at different stages as the KHI is operating. Inset shows the X-Y directions for the 2D plots in the upper two rows.

One must indeed note that simulations included in this study are performed using a specific set of parameters supported by the data, yet there are many adjustable parameters that *cannot* be fully constrained (e.g., scale length and inertial capacitance). Additionally, there is a quite large parameter space to explore for fully characterizing nonlinear-stage KHI behavior. Nevertheless, the simulations show that significant density irregularities and phase variations (and thus, σ_ϕ) can arise from such a representative case of sheared-flow, supporting that KHI is likely significantly contributing in situations similar to the one presented, provided short gradient length-scales.

Previous studies (Oksavik et al., 2011; Rinne et al., 2007) have identified that RFEs were regular features of the cusp, generally most frequent for IMF $|B_y| > |B_z|$, that is, when IMF is dominated by B_y (as it is the case for the current study). KHI may thus also be a common feature of the cusp, and a question arising is whether there are any particular conditions in the solar wind that may give preference to, for example, KHI over GDI. Indeed, this suggests that IMF B_y can potentially play an important role for when flow shears form in the cusp and, consequently, when the KHI mechanism is most likely to operate. However, it needs to be investigated further in future studies whether different mechanisms (e.g., KHI and GDI or a certain combination of both) actually dominate under different solar wind conditions.

6. Conclusion

We presented observations of a narrow cusp flow channel and RFE, that is, exemplary multiscale phenomena: they result from magnetosphere-ionosphere coupling, are embedded in a larger scale flow pattern, and involve structures ranging from several kilometers to tens of meters. We provided evidence that strong phase scintillation ($\sigma_\phi > 0.5$ rad) could arise from such events, confirming that they are important in the context of impacts of space weather on technology. We compared in more detail different sources of free energy observed through 2D maps of density, velocity, and temperatures, obtained from the scanning capabilities of ESR, with scintillation indices detected from a network of four GNSS receivers around Svalbard. We found that the strongest phase scintillation coincided with enhanced SuperDARN spectral width and were localized on the poleward side of the flow channel, in a region of sheared flow with structured low-energy particle precipitation. Furthermore, the presence of enhanced electron density appeared to be a prerequisite for the strongest scintillation to arise.

Observations were placed in context of the KHI due to velocity shear observations and the prevalence of inhomogeneous flows near the cusp (e.g., Carlson et al., 2008; Heppner et al., 1993; Moen et al., 2008;

Acknowledgments
This research is part of the 4DSpace Strategic Research Initiative at University of Oslo. The Research Council of Norway has provided financial support to AS, JM (grant 275653), KO (grants 212014 and 223252), and LBNC and YJ (grant 235655). KD's work on investigating scintillation through KHI structures was supported by NSF CAREER grant AGS-1848207. The work by MH was supported by NASA grant NNX15AT31G. EISCAT is an international association supported by research organizations in China (CRIRP), Finland (SA), Japan (NIPR and STEL), Norway (NFR), Sweden (VR), and the United Kingdom (NERC). Data from EISCAT can be obtained from the Madrigal database (https://portal.eiscat.se/madrigal/). GPS TEC data products and access through the Madrigal distributed data system are provided to the community (http://www.openmadrigal.org) by the Massachusetts Institute of Technology (MIT) under support from US National Science Foundation grant AGS-1242204. Data for TEC processing is provided from the following organizations: UNAVCO, Scripps Orbit and Permanent Array Center, Institut Geographique National, France, International GNSS Service, The Crustal Dynamics Data Information System (CDDIS), National Geodetic Survey, Instituto Brasileiro de Geografia e Estatística, RAMSAC CORS of Instituto Geográfico Nacional de la República Argentina, Arecibo Observatory, Low-Latitude Ionospheric Sensor Network (LISN), Topcon Positioning Systems, Inc., Canadian High Arctic Ionospheric Network, Centro di Ricerche Sismologiche, SystÃme d'Observation du Niveau des Eaux Littorales (SONEL), RENAG: REseau NAtional GPS permanent, GeoNet - the official source of geological hazard information for New Zealand, GNSS Reference Networks, Finnish Meteorological Institute, and SWEPOS - Sweden. Access to these data is provided by madrigal network (https://cedar.openmadrigal.org/). GEMINI is a free, open-source software and can be downloaded from GitHub (https://github.com/gemini3d/). Build instructions, example simulations, and documentation are also included on this website. Development of GEMINI was supported under NSF CAREER grant AGS-1255181. Movies of the GEMINI simulations shown in the figures are included in the supporting information while the GNSS data (Oksavik et al., 2020), the GEMINI code release used for this manuscript, incl. GEMINI (Hirsch et al., 2020), GEMINI-scripts (Zettergren & Hirsch, 2020), GEMINI-examples (Zettergren & Hirsch, 2020), GEMINI-docs

Oksavik et al., 2004b, 2005; Rinne et al., 2007), where phase scintillations peak (Jin et al., 2015, 2017; Prikryl et al., 2015). We do not rule out GDI or precipitation (or alternative possibilities) as playing a role in the scintillation for the specific event. Instead, we showed that, under reasonable assumptions consistent with the data, KHI can relatively easily explain the creation of density irregularities within minutes. KHI is thus likely under conditions similar to the ones observed, which are common in the cusp (Oksavik et al., 2011; Rinne et al., 2007). This is the case even with considerations for Hall currents and recombination, which are included in our model but not the original KHI modeling study of Keskinen et al. (1988). Thus, we have performed the first quantitative, nonlinear analysis suggesting KHI as a process involved in the irregularity generation in the cusp.

Finally, this study shows that wide field of view incoherent scatter radar experiments (e.g., our ESR fast azimuth sweeps or future volumetric measurements with EISCAT3D; (McCrea et al., 2015)) have great potential for investigating space weather phenomena in the ionosphere. It also illustrates some of the capabilities of GEMINI-SIGMA modeling for future parametric studies to constrain KHI and to compare its relative importance with respect to concurrent mechanisms (e.g., GDI and precipitation). This study has certainly demonstrated that compared to GDI, KHI displays a specific pattern in scintillation occurrence, that is, with respect to the density boundaries, vortices, and small-scale structures developing around those vortices.

Future modeling work will need to focus more on how KHI develops in the nonlinear stage in situations representative of different boundary layer widths (ℓ) and different levels of ion-neutral and ionospheric-magnetospheric coupling. An assessment of how these density irregularities manifest as different scintillation signatures will also be revealing. The type of seeding used to trigger the instability will also affect the character of the response, viz. we used white noise to seed the simulations, while Keskinen et al. (1988) used single modes (eigenfunctions) to seed their instability. In particular, we identify the need to examine realistic initial conditions (nonuniform density and velocity) and structured particle precipitation as a seed process for KHI and related instabilities (e.g., Moen et al., 2012; Oksavik et al., 2012), and develop mixed-mode examples of simulations.

Observationally, it is necessary, moving forward, to quantify the scale lengths present in RFEs and other ionospheric shear flow events with high-resolution instruments. These are of importance to understanding cusp scintillation and greatly impact our simulation results. Additionally, a better statistical characterization of conditions accompanying sheared flows (precipitation, typical velocities, and shears) will also help inform and constrain parameter modeling efforts to understand the relation of KHI to scintillation in the cusp.

References

Alfonsi, L., Spogli, L., Tong, J. R., Franceschi, G. D., Romano, V., Bourdillon, A., et al. (2011). GPS scintillation and TEC gradients at equatorial latitudes in April 2006. *Advances in Space Research*, *47*(10), 1750–1757. GNSS Remote Sensing-2, https://doi.org/10.1016/j.asr.2010.04.02

Baker, K. B., & Wing, S. (1989). A new magnetic coordinate system for conjugate studies at high latitudes. *Journal of Geophysical Research*, *94*(A7), 9139–9143. https://doi.org/10.1029/JA094iA07p09139

Basu, S., Basu, S., Chaturvedi, P. K., & Bryant Jr, C. M. (1994). Irregularity structures in the cusp/cleft and polar cap regions. *Radio Science*, *29*(1), 195–207. https://doi.org/10.1029/93RS01515

Basu, S., Basu, S., MacKenzie, E., Fougere, P. F., Coley, W. R., Maynard, N. C., et al. (1988). Simultaneous density and electric field fluctuation spectra associated with velocity shears in the auroral oval. *Journal of Geophysical Research*, *93*(A1), 115–136. https://doi.org/10.1029/JA093iA01p00115

Basu, S., Basu, S., Senior, C., Weimer, D., Nielsen, E., & Fougere, P. F. (1986). Velocity shears and sub-km scale irregularities in the nighttime auroral F-region. *Geophysical Research Letters*, *13*(2), 101–104. https://doi.org/10.1029/GL013i002p00101

Beach, T. L. (2006). Perils of the GPS phase scintillation index (σ_ϕ). *Radio Science*, *41*, RS5S31. https://doi.org/10.1029/2005RS003356

Blelly, P., & Schunk, R. (1993). A comparative study of the time-dependent standard 8-, 13- and 16-moment transport formulations of the polar wind. In *Annales geophysicae*, *11*, pp. 443–469.

Briggs, B. H., & Parkin, I. A. (1963). On the variation of radio star and satellite scintillations with zenith angle. *Journal of Atmospheric and Terrestrial Physics*, *25*(6), 339–366. https://doi.org/10.1016/0021-9169(63)90150-8

Cargill, P. J., Lavraud, B., Owen, C. J., Grison, B., Dunlop, M. W., Cornilleau-Wehrlin, N., et al. (2005). Cluster at the Magnetospheric Cusps. In Paschmann, G., Schwartz, S. J., Escoubet, C. P., & Haaland, S. (Eds.), *Outer Magnetospheric Boundaries: Cluster Results* pp. 321–366). Dordrecht: Springer Netherlands. https://doi.org/10.1007/1-4020-4582-4n_10

Carlson, H. C. (2012). Sharpening our thinking about polar cap ionospheric patch morphology, research, and mitigation techniques. *Radio Science*, *47*, RS0L21. https://doi.org/10.1029/2011RS004946

Carlson, H. C., Oksavik, K., & Moen, J. (2008). On a new process for cusp irregularity production. *Annales Geophysicae*, *26*(9), 2871–2885.

Carlson, H. C., Oksavik, K., Moen, J., van Eyken, A. P., & Guio, P. (2002). ESR mapping of polar-cap patches in the dark cusp. *Geophysical Research Letters*, *29*(10), 24–1–24–4. https://doi.org/10.1029/2001GL014087

Carlson, H. C., Pedersen, T., Basu, S., Keskinen, M., & Moen, J. (2007). Case for a new process, not mechanism, for cusp irregularity production. *Journal of Geophysical Research*, *112*, A11304. https://doi.org/10.1029/2007JA012384

(Zettergren & Hirsch, 2020), and the outputs from the GEMINI-SIGMA combination (Deshpande et al., 2020) are placed in repositories. MZ and KD gratefully acknowledge use of the ERAU Vega High-Performance Computing Cluster for running simulations presented in this paper. MZ would like to thank Dr. Michael Hirsch for guidance in how to set up an archive DOIs with connections to GitHub. The authors acknowledge the use of SuperDARN data. SuperDARN is a collection of radars funded by national scientific funding agencies of Australia, Canada, China, France, Japan, South Africa, the United Kingdom, and the United States of America. The OMNI solar wind data, the DMSP SSJ 5, and the SSIES data are provided through NASA's Space Physics Data Facility (SPDF) (https://cdaweb.gsfc.nasa.gov/index.html/). DMSP SSJ data can also be accessed at the National Oceanic and Atmospheric Administration (NOAA) National Centers for Environmental Information (NCEI) (https://www.ngdc.noaa.gov/stp/satellite/dmsp/). Finally, the authors gratefully acknowledge the helpful comments from the reviewers.

Chaston, C. C., Carlson, C. W., McFadden, J. P., Ergun, R. E., & Strangeway, R. J. (2007). How important are dispersive Alfvé waves for auroral particle acceleration? *Geophysical Research Letters*, *34*, L07101. https://doi.org/10.1029/2006GL029144

Chisham, G., Lester, M., Milan, S. E., Freeman, M. P., Bristow, W. A., Grocott, A., et al. (2007). A decade of the Super Dual Auroral Radar Network (SuperDARN): Scientific achievements, new techniques and future directions. *Surveys in Geophysics*, *28*(1), 33–109. https://doi.org/10.1007/s10712-007-9017-8

Clauer, C. R. (2003). Ionospheric observations of waves at the inner edge of the low latitude boundary layer. In *Earth's low-latitude boundary layer*, American Geophysical Union (AGU), pp. 297–309. https://doi.org/10.1029/133GM30

Clausen, L. B. N., Moen, J. I., Hosokawa, K., & Holmes, J. M. (2016). GPS scintillations in the high latitudes during periods of dayside and nightside reconnection. *Journal of Geophysical Research: Space Physics*, *121*, 3293–3309. https://doi.org/10.1002/2015JA022199

Deshpande, K. B., Bust, G. S., Clauer, C. R., Rino, C. L., & Carrano, C. S. (2014). Satellite-beacon Ionospheric-scintillation Global Model of the upper Atmosphere (SIGMA) I: High latitude sensitivity study of the model parameters. *Journal of Geophysical Research: Space Physics*, *119*, 4026–4043. https://doi.org/10.1002/2013JA019699

Deshpande, K., Spicher, A., Jin, Y., Oksavik, K., Zettergren, M. D., Clausen, L. B. N., et al. (2020). GEMINI-SIGMA output replication data for: "On the production of ionospheric irregularities via Kelvin-Helmholtz instability associated with cusp flow channels". https://doi.org/10.18710/5IYSKV

Deshpande, K. B., & Zettergren, M. D. (2019). Satellite-beacon Ionospheric-scintillation Global Model of the Upper Atmosphere (SIGMA) III: Scintillation simulation using a physics-based plasma model. *Geophysical Research Letters*, *46*, 4564–4572. https://doi.org/10.1029/2019GL082576

Diloy, P.-Y., Robineau, A., Lilensten, J., Blelly, P.-L., & Fontanari, J. (1996). A numerical model of the ionosphere, including the E-region above EISCAT. In *Annales geophysicae*, *14*, pp. 191–200.

Doe, R. A., Kelly, J. D., & Sánchez, E. R. (2001). Observations of persistent dayside F region electron temperature enhancements associated with soft magnetosheathlike precipitation. *Journal of Geophysical Research*, *106*(A3), 3615–3630. https://doi.org/10.1029/2000JA000186

Dyson, P. L., & Winningham, J. D. (1974). Top side ionospheric spread F and particle precipitation in the day side magnetospheric clefts. *Journal of Geophysical Research*, *79*(34), 5219–5230. https://doi.org/10.1029/JA079i034p05219

Earle, G. D., Kelley, M. C., & Ganguli, G. (1989). Large velocity shears and associated electrostatic waves and turbulence in the auroral F region. *Journal of Geophysical Research*, *94*(A11), 15,321–15,333. https://doi.org/10.1029/JA094iA11p15321

Fang, X., Randall, C. E., Lummerzheim, D., Solomon, S. C., Mills, M. J., Marsh, D. R., et al. (2008). Electron impact ionization: A new parameterization for 100 eV to 1 MeV electrons. *Journal of Geophysical Research*, *113*, A09311. https://doi.org/10.1029/2008JA013384

Forsythe, V. V., & Makarevich, R. A. (2018). Statistical analysis of the electron density gradients in the polar cap F region using the resolute bay incoherent scatter radar north. *Journal of Geophysical Research: Space Physics*, *123*, 4066–4079. https://doi.org/10.1029/2017JA025156

Forte, B., Coleman, C., Skone, S., Häggström, I., Mitchell, C., Da Dalt, F., et al. (2017). Identification of scintillation signatures on GPS signals originating from plasma structures detected with EISCAT incoherent scatter radar along the same line of sight. *Journal of Geophysical Research: Space Physics*, *122*, 916–931. https://doi.org/10.1002/2016JA023271

Forte, B., & Radicella, S. M. (2002). Problems in data treatment for ionospheric scintillation measurements. *Radio Science*, *37*(6), 8–1–8–5. https://doi.org/10.1029/2001RS002508

Fremouw, E. J., Leadabrand, R. L., Livingston, R. C., Cousins, M. D., Rino, C. L., Fair, B. C., & Long, R. A. (1978). Early results from the DNA Wideband satellite experiment—Complex-signal scintillation. *Radio Science*, *13*(1), 167–187. https://doi.org/10.1029/RS013i001p00167

Ganguli, G., Keskinen, M. J., Romero, H., Heelis, R., Moore, T., & Pollock, C. (1994). Coupling of microprocesses and macroprocesses due to velocity shear: An application to the low-altitude ionosphere. *Journal of Geophysical Research*, *99*(A5), 8873–8889. https://doi.org/10.1029/93JA03181

Gondarenko, N. A., & Guzdar, P. N. (2004). Plasma patch structuring by the nonlinear evolution of the gradient drift instability in the high-latitude ionosphere. *Journal of Geophysical Research*, *109*, A09301. https://doi.org/10.1029/2004JA010504

Hairston, M. (2019). A short introduction to the DMSP SSIES-3 quality flags and how to use them. SPDF technical document, https://spdf.gsfc.nasa.gov/pub/data/dmsp/documents/ssies/SSIES-3_qualityflags_Sept2019.pdf.

Hardy, D. A., Holeman, E. G., Burke, W. J., Gentile, L. C., & Bounar, K. H. (2008). Probability distributions of electron precipitation at high magnetic latitudes. *Journal of Geophysical Research*, *113*, A06305. https://doi.org/10.1029/2007JA012746

Heppner, J. P., Liebrecht, M. C., Maynard, N. C., & Pfaff, R. F. (1993). High-latitude distributions of plasma waves and spatial irregularities from DE 2 alternating current electric field observations. *Journal of Geophysical Research*, *98*(A2), 1629–1652. https://doi.org/10.1029/92JA01836

Hey, J. S., Parsons, S. J., & Phillips, J. W. (1946). Fluctuations in cosmic radiation at radio-frequencies. *Nature*, *158*, 234. https://doi.org/10.1038/158234a0

Hirsch, M., Zettergren, M. D., & Grubbs, G. (2020). gemini3d/GEMINI: KHI JGR version of code. https://doi.org/10.5281/zenodo.3647580

Huba, J. D., Mitchell, H. G., Keskinen, M. J., Fedder, J. A., Satyanarayana, P., & Zalesak, S. T. (1988). Simulations of plasma structure evolution in the high-latitude ionosphere. *Radio Science*, *23*(4), 503–512. https://doi.org/10.1029/RS023i004p00503

Jin, Y., Miloch, W. J., Moen, J. I., & Clausen, LasseB. N. (2018b). Solar cycle and seasonal variations of the GPS phase scintillation at high latitudes. *Journal of Space Weather and Space Climate*, *8*, A48. https://doi.org/10.1051/swsc/2018034

Jin, Y., Moen, J., & Miloch, W. J. (2014). GPS scintillation effects associated with polar cap patches and substorm auroral activity: Direct comparison. *Journal of Space Weather and Space Climate*, *4*, A23. https://doi.org/10.1051/swsc/2014019

Jin, Y., Moen, J. I., & Miloch, W. J. (2015). On the collocation of the cusp aurora and the GPS phase scintillation: A statistical study. *Journal of Geophysical Research: Space Physics*, *120*, 9176–9191. https://doi.org/10.1002/2015JA021449

Jin, Y., Moen, J. I., Miloch, W. J., Clausen, L. B. N., & Oksavik, K. (2016). Statistical study of the GNSS phase scintillation associated with two types of auroral blobs. *Journal of Geophysical Research: Space Physics*, *121*, 4679–4697. https://doi.org/10.1002/2016JA022613

Jin, Y., Moen, J. I., Oksavik, K., Spicher, A., Clausen, L. B. N., & Miloch, W. J. (2017). GPS scintillations associated with cusp dynamics and polar cap patches. *Journal of Space Weather and Space Climate*, *7*, A23. https://doi.org/10.1051/swsc/2017022

Jin, Y., Moen, J. I., Spicher, A., Oksavik, K., Miloch, W. J., Clausen, L. B. N., et al. (2019b). Simultaneous rocket and scintillation observations of plasma irregularities associated with a reversed flow event in the cusp ionosphere. *Journal of Geophysical Research: Space Physics*, *124*, 7098–7111. https://doi.org/10.1029/2019JA026942

Jin, Y., Spicher, A., Xiong, C., Clausen, L. B. N., Kervalishvili, G., Stolle, C., & Miloch, W. J. (2019). Ionospheric plasma irregularities characterized by the swarm satellites: Statistics at high latitudes. *Journal of Geophysical Research: Space Physics*, *124*, 1262–1282. https://doi.org/10.1029/2018JA026063

Kelley, M. C., & Carlson, C. W. (1977). Observations of intense velocity shear and associated electrostatic waves near an auroral arc. *Journal of Geophysical Research*, *82*(16), 2343–2348. https://doi.org/10.1029/JA082i016p02343

Kelley, M. C., Vickrey, J. F., Carlson, C. W., & Torbert, R. (1982). On the origin and spatial extent of high-latitude F region irregularities. *Journal of Geophysical Research*, *87*(A6), 4469–4475. https://doi.org/10.1029/JA087iA06p04469

Keskinen, M. J., Mitchell, H. G., Fedder, J. A., Satyanarayana, P., Zalesak, S. T., & Huba, J. D. (1988). Nonlinear evolution of the Kelvin-Helmholtz instability in the high-latitude ionosphere. *Journal of Geophysical Research*, *93*(A1), 137–152. https://doi.org/10.1029/JA093iA01p00137

Keskinen, M. J., & Ossakow, S. L. (1983). Theories of high-latitude ionospheric irregularities: A review. *Radio Science*, *18*(6), 1077–1091. https://doi.org/10.1029/RS018i006p01077

Kilcommons, L. M., Redmon, R. J., & Knipp, D. J. (2017). A new DMSP magnetometer and auroral boundary data set and estimates of field-aligned currents in dynamic auroral boundary coordinates. *Journal of Geophysical Research: Space Physics*, *122*, 9068–9079. https://doi.org/10.1002/2016JA023342

King, J. H., & Papitashvili, N. E. (2005). Solar wind spatial scales in and comparisons of hourly Wind and ACE plasma and magnetic field data. *Journal of Geophysical Research*, *110*, A02104. https://doi.org/10.1029/2004JA010649

Kintner, P. M., Ledvina, B. M., & de Paula, E. R. (2007). GPS and ionospheric scintillations. *Space Weather*, *5*, S09003. https://doi.org/10.1029/2006SW000260

Kintner, P. M., & Seyler, C. E. (1985). The status of observations and theory of high latitude ionospheric and magnetospheric plasma turbulence. *Space Science Reviews*, *41*(1), 91–129. https://doi.org/10.1007/BF00241347

Labelle, J., Sica, R. J., Kletzing, C., Earle, G. D., Kelley, M. C., Lummerzheim, D., et al. (1989). Ionization from soft electron precipitation in the auroral F region. *Journal of Geophysical Research*, *94*(A4), 3791–3798. https://doi.org/10.1029/JA094iA04p03791

Lamarche, L. J., & Makarevich, R. A. (2017). Radar observations of density gradients, electric fields, and plasma irregularities near polar cap patches in the context of the gradient-drift instability. *Journal of Geophysical Research: Space Physics*, *122*, 3721–3736. https://doi.org/10.1002/2016JA023702

Linson, L. M., & Workman, J. B. (1970). Formation of striations in ionospheric plasma clouds. *Journal of Geophysical Research*, *75*(16), 3211–3219. https://doi.org/10.1029/JA075i016p03211

Makarevich, R. A. (2014). Symmetry considerations in the two-fluid theory of the gradient drift instability in the lower ionosphere. *Journal of Geophysical Research: Space Physics*, *119*, 7902–7913. https://doi.org/10.1002/2014JA020292

Makarevich, R. A. (2017). Critical density gradients for small-scale plasma irregularity generation in the E and F regions. *Journal of Geophysical Research: Space Physics*, *122*, 9588–9602. https://doi.org/10.1002/2017JA024393

Mannucci, A. J., Wilson, B. D., & Edwards, C. D. (1993). A new method for monitoring the Earth's ionospheric total electron content using the GPS global network. In *Proceedings of the 6th International Technical Meeting of the Satellite Division of The Institute of Navigation (ION GPS 1993), Salt Lake City, UT*, pp. 1323–1332.

McCaffrey, A. M., & Jayachandran, P. T. (2019). Determination of the refractive contribution to GPS phase "scintillation". *Journal of Geophysical Research: Space Physics*, *124*, 1454–1469. https://doi.org/10.1029/2018JA025759

McCrea, I., Aikio, A., Alfonsi, L., Belova, E., Buchert, S., Clilverd, M., et al. (2015). The science case for the EISCAT_3D radar. *Progress in Earth and Planetary Science*, *2*(1), 21. https://doi.org/10.1186/s40645-015-0051-8

Millward, G. H., Moffett, R. J., Balmforth, H. F., & Rodger, A. S. (1999). Modeling the ionospheric effects of ion and electron precipitation in the cusp. *Journal of Geophysical Research*, *104*(A11), 24,603–24,612. https://doi.org/10.1029/1999JA900249

Mitchell, C. N., Alfonsi, L., De Franceschi, G., Lester, M., Romano, V., & Wernik, A. W. (2005). GPS TEC and scintillation measurements from the polar ionosphere during the October 2003 storm. *Geophysical Research Letters*, *32*, L12S03. https://doi.org/10.1029/2004GL021644

Moen, J., Oksavik, K., Abe, T., Lester, M., Saito, Y., Bekkeng, T. A., & Jacobsen, K. S. (2012). First in-situ measurements of HF radar echoing targets. *Geophysical Research Letters*, *39*, L07104. https://doi.org/10.1029/2012GL051407

Moen, J., Oksavik, K., Alfonsi, L., Daabakk, Y., Romano, V., & Spogli, L. (2013). Space weather challenges of the polar cap ionosphere. *Journal of Space Weather and Space Climate*, *3*, A02. https://doi.org/10.1051/swsc/2013025

Moen, J., Rinne, Y., Carlson, H. C., Oksavik, K., Fujii, R., & Opgenoorth, H. (2008). On the relationship between thin Birkeland current arcs and reversed flow channels in the winter cusp/cleft ionosphere. *Journal of Geophysical Research*, *113*, A09220. https://doi.org/10.1029/2008JA013061

Moen, J., Walker, I. K., Kersley, L., & Milan, S. E. (2002). On the generation of cusp HF backscatter irregularities. *Journal of Geophysical Research*, *107*(A4), SIA 3–1–SIA 3–5. https://doi.org/10.1029/2001JA000111

Mushini, S. C., Jayachandran, P. T., Langley, R. B., MacDougall, J. W., & Pokhotelov, D. (2012). Improved amplitude- and phase-scintillation indices derived from wavelet detrended high-latitude GPS data. *GPS Solutions*, *16*(3), 363–373. https://doi.org/10.1007/s10291-011-0238-4

Oksavik, K., Moen, J., & Carlson, H. C. (2004a). High-resolution observations of the small-scale flow pattern associated with a poleward moving auroral form in the cusp. *Geophysical Research Letters*, *31*, L11807. https://doi.org/10.1029/2004GL019838

Oksavik, K., Moen, J., Carlson, H. C., Greenwald, R. A., Milan, S. E., Lester, M., et al. (2005). Multi-instrument mapping of the small-scale flow dynamics related to a cusp auroral transient. *Annales Geophysicae*, *23*(7), 2657–2670. https://doi.org/10.5194/angeo-23-2657-2005

Oksavik, K., Moen, J., Lester, M., Bekkeng, T. A., & Bekkeng, J. K. (2012). In situ measurements of plasma irregularity growth in the cusp ionosphere. *Journal of Geophysical Research*, *117*, A11301. https://doi.org/10.1029/2012JA017835

Oksavik, K., Moen, J. I., Rekaa, E. H., Carlson, H. C., & Lester, M. (2011). Reversed flow events in the cusp ionosphere detected by SuperDARN HF radars. *Journal of Geophysical Research*, *116*, A12303. https://doi.org/10.1029/2011JA016788

Oksavik, K., Ruohoniemi, J. M., Greenwald, R. A., Baker, J. B. H., Moen, J., Carlson, H. C., et al. (2006). Observations of isolated polar cap patches by the European Incoherent Scatter (EISCAT) Svalbard and Super Dual Auroral Radar Network (SuperDARN) Finland radars. *Journal of Geophysical Research*, *111*, A05310. https://doi.org/10.1029/2005JA011400

Oksavik, K., Soraas, F., Moen, J., Pfaff, R., Davies, J. A., & Lester, M. (2004b). Simultaneous optical, CUTLASS HF radar, and FAST spacecraft observations: Signatures of boundary layer processes in the cusp. *Annales Geophysicae*, *22*(2), 511–525. https://doi.org/10.5194/angeo-22-511-2004

Oksavik, K., Spicher, A., Deshpande, K., Jin, Y., Zettergren, M. D., Clausen, L. B. N., et al. (2020). GNSS replication data for: "On the production of ionospheric irregularities via Kelvin-Helmholtz instability associated with cusp flow channels". https://doi.org/10.18710/LOIWIU

Oksavik, K., van der Meeren, C., Lorentzen, D. A., Baddeley, L. J., & Moen, J. (2015). Scintillation and loss of signal lock from poleward moving auroral forms in the cusp ionosphere. *Journal of Geophysical Research: Space Physics*, *120*, 9161–9175. https://doi.org/10.1002/2015JA021528

Phelps, A. D. R., & Sagalyn, R. C. (1976). Plasma density irregularities in the high-latitude top side ionosphere. *Journal of Geophysical Research*, *81*(4), 515–523. https://doi.org/10.1029/JA081i004p00515

Pinnock, M., Rodger, A. S., Dudeney, J. R., Baker, K. B., Newell, P. T., Greenwald, R. A., & Greenspan, M. E. (1993). Observations of an enhanced convection channel in the cusp ionosphere. *Journal of Geophysical Research*, *98*(A3), 3767–3776. https://doi.org/10.1029/92JA01382

Prikryl, P., Jayachandran, P. T., Chadwick, R., & Kelly, T. D. (2015). Climatology of GPS phase scintillation at northern high latitudes for the period from 2008 to 2013. *Annales Geophysicae*, *33*(5), 531–545. https://doi.org/10.5194/angeo-33-531-2015

Prikryl, P., Jayachandran, P. T., Mushini, S. C., & Chadwick, R. (2011). Climatology of GPS phase scintillation and HF radar backscatter for the high-latitude ionosphere under solar minimum conditions. *Annales Geophysicae*, *29*(2), 377–392. https://doi.org/10.5194/angeo-29-377-2011

Redmon, R. J., Denig, W. F., Kilcommons, L. M., & Knipp, D. J. (2017). New DMSP database of precipitating auroral electrons and ions. *Journal of Geophysical Research: Space Physics*, *122*, 9056–9067. https://doi.org/10.1002/2016JA023339

Rees, M. H. (1963). Auroral ionization and excitation by incident energetic electrons. *Planetary and Space Science*, *11*(10), 1209–1218. https://doi.org/10.1016/0032-0633(63)90252-6

Rich, F. J. (1994b). Users Guide for the Topside Ionospheric Plasma Monitor (SSIES, SSIES-2, and SSIES-3) on Spacecraft of the Defense Meteorological Satellite Program (DMSP). Volume I: Technical Description. Phillips Laboratory Technical Report PL-TR-94-2187, https://satdat.ngdc.noaa.gov/dmsp/docs/Rich-1994-UsersGuideSSIES-1SSIES-2SSIES-3-PL-TR-94-2187.pdf.

Rich, F. J., & Hairston, M. (1994). Large-scale convection patterns observed by DMSP. *Journal of Geophysical Research*, *99*(A3), 3827–3844. https://doi.org/10.1029/93JA03296

Richards, P., Fennelly, J., & Torr, D. (1994). EUVAC: A solar EUV flux model for aeronomic calculations. *Journal of Geophysical Research*, *99*(A5), 8981–8992.

Rideout, W., & Coster, A. (2006). Automated GPS processing for global total electron content data. *GPS Solutions*, *10*(3), 219–228. https://doi.org/10.1007/s10291-006-0029-5

Rinne, Y., Moen, J., Oksavik, K., & Carlson, H. C. (2007). Reversed flow events in the winter cusp ionosphere observed by the European Incoherent Scatter (EISCAT) Svalbard radar. *Journal of Geophysical Research*, *112*, A10313. https://doi.org/10.1029/2007JA012366

Rino, C. L. (1979). A power law phase screen model for ionospheric scintillation: 1. Weak scatter. *Radio Science*, *14*(6), 1135–1145. https://doi.org/10.1029/RS014i006p01135

Ruohoniemi, J. M., Greenwald, R. A., Baker, K. B., Villain, J. P., Hanuise, C., & Kelly, J. (1989). Mapping high-latitude plasma convection with coherent HF radars. *Journal of Geophysical Research*, *94*(A10), 13,463–13,477. https://doi.org/10.1029/JA094iA10p13463

Schunk, R. (1977). Mathematical structure of transport equations for multispecies flows. *Reviews of Geophysics*, *15*(4), 429–445.

Semeter, J., Mrak, S., Hirsch, M., Swoboda, J., Akbari, H., Starr, G., et al. (2017). GPS signal corruption by the discrete aurora: Precise measurements from the Mahali experiment. *Geophysical Research Letters*, *44*, 9539–9546. https://doi.org/10.1002/2017GL073570

Simon, A. (1963). Instability of a partially ionized plasma in crossed electric and magnetic fields. *The Physics of Fluids*, *6*(3), 382–388. https://doi.org/10.1063/1.1706743

Solomon, S. C., & Qian, L. (2005). Solar extreme-ultraviolet irradiance for general circulation models. *Journal of Geophysical Research*, *110*, A10306. https://doi.org/10.1029/2005JA011160

Southwood, D. J. (1987). The ionospheric signature of flux transfer events. *Journal of Geophysical Research*, *92*(A4), 3207–3213. https://doi.org/10.1029/JA092iA04p03207

Spicher, A., Ilyasov, A. A., Miloch, W. J., Chernyshov, A. A., Clausen, L. B. N., Moen, J. I., et al. (2016). Reverse flow events and small-scale effects in the cusp ionosphere. *Journal of Geophysical Research: Space Physics*, *121*, 10,466–10,480. https://doi.org/10.1002/2016JA022999

Spicher, A., Miloch, W. J., Clausen, L. B. N., & Moen, J. I. (2015). Plasma turbulence and coherent structures in the polar cap observed by the ICI-2 sounding rocket. *Journal of Geophysical Research: Space Physics*, *120*, 10,959–10,978. https://doi.org/10.1002/2015JA021634

Spogli, L., Alfonsi, L., De Franceschi, G., Romano, V., Aquino, M. H. O., & Dodson, A. (2009). Climatology of GPS ionospheric scintillations over high and mid-latitude European regions. *Annales Geophysicae*, *27*(9), 3429–3437. https://doi.org/10.5194/angeo-27-3429-2009

St-Maurice, J.-P., & Laneville, P. (1998). Reaction rate of O+ with O2, N2, and NO under highly disturbed auroral conditions. *Journal of Geophysical Research*, *103*(A8), 17,519–17,521.

Thébault, E., Finlay, C. C., Beggan, C. D., Alken, P., Aubert, J., Barrois, O., et al. (2015). International geomagnetic reference field: The 12th generation. *Earth, Planets and Space*, *67*(1), 79. https://doi.org/10.1186/s40623-015-0228-9

Thomas, E. G., Baker, J. B. H., Ruohoniemi, J. M., Clausen, L. B. N., Coster, A. J., Foster, J. C., & Erickson, P. J. (2013). Direct observations of the role of convection electric field in the formation of a polar tongue of ionization from storm enhanced density. *Journal of Geophysical Research: Space Physics*, *118*, 1180–1189. https://doi.org/10.1002/jgra.50116

Tsunoda, R. T. (1988). High-latitude F region irregularities: A review and synthesis. *Reviews of Geophysics*, *26*(4), 719–760. https://doi.org/10.1029/RG026i004p00719

Valladares, C. E., & Carlson Jr, H. C. (1991). The electrodynamic, thermal, and energetic character of intense Sun-aligned arcs in the polar cap. *Journal of Geophysical Research*, *96*(A2), 1379–1400. https://doi.org/10.1029/90JA01765

Van Dierendonck, A. J., Klobuchar, J., & Hua, Q. (1993). Ionospheric scintillation monitoring using commercial single frequency C/A code receivers. In *Proceedings of the 6th International Technical Meeting of the Satellite Division of the Institute of Navigation (ion gps 1993)*, Salt Lake City, UT, September 1993, pp. 1333–1342.

van der Meeren, C., Oksavik, K., Lorentzen, D., Moen, J. I., & Romano, V. (2014). GPS scintillation and irregularities at the front of an ionization tongue in the nightside polar ionosphere. *Journal of Geophysical Research: Space Physics*, *119*, 8624–8636. https://doi.org/10.1002/2014JA020114

van der Meeren, C., Oksavik, K., Lorentzen, D. A., Paxton, L. J., & Clausen, L. B. N. (2016). Scintillation and irregularities from the nightside part of a Sun-aligned polar cap arc. *Journal of Geophysical Research: Space Physics*, *121*, 5723–5736. https://doi.org/10.1002/2016JA022708

van der Meeren, C., Oksavik, K., Lorentzen, D. A., Rietveld, M. T., & Clausen, L. B. N. (2015). Severe and localized GNSS scintillation at the poleward edge of the nightside auroral oval during intense substorm aurora. *Journal of Geophysical Research: Space Physics*, *120*, 10,607–10,621. https://doi.org/10.1002/2015JA021819

Vierinen, J., Coster, A. J., Rideout, W. C., Erickson, P. J., & Norberg, J. (2016). Statistical framework for estimating GNSS bias. *Atmospheric Measurement Techniques*, *9*(3), 1303–1312. https://doi.org/10.5194/amt-9-1303-2016

Vontrat-Reberac, A., Fontaine, D., Blelly, P.-L., & Galand, M. (2001). Theoretical predictions of the effect of cusp and dayside precipitation on the polar ionosphere. *Journal of Geophysical Research*, *106*(A12), 28,857–28,865. https://doi.org/10.1029/2001JA900131

Wang, Y., Zhang, Q.-H., Jayachandran, P. T., Lockwood, M., Zhang, S.-R., Moen, J., et al. (2016). A comparison between large-scale irregularities and scintillations in the polar ionosphere. *Geophysical Research Letters*, *43*, 4790–4798. https://doi.org/10.1002/2016GL069230

Wang, Y., Zhang, Q.-H., Jayachandran, P. T., Moen, J., Xing, Z.-Y., Chadwick, R., et al. (2018). Experimental evidence on the dependence of the standard GPS Phase Scintillation Index on the ionospheric plasma drift around noon sector of the polar ionosphere. *Journal of Geophysical Research: Space Physics*, *123*, 2370–2378. https://doi.org/10.1002/2017JA024805

Wannberg, G., Wolf, I., Vanhainen, L.-G., Koskenniemi, K., Röttger, J., Postila, M., et al. (1997). The EISCAT Svalbard radar: A case study in modern incoherent scatter radar system design. *Radio Science*, *32*(6), 2283–2307. https://doi.org/10.1029/97RS01803

Weber, E. J., Buchau, J., Moore, J. G., Sharber, J. R., Livingston, R. C., Winningham, J. D., & Reinisch, B. W. (1984). F layer ionization patches in the polar cap. *Journal of Geophysical Research*, *89*(A3), 1683–1694. https://doi.org/10.1029/JA089iA03p01683

Weber, E. J., Kelley, M. C., Ballenthin, J. O., Basu, S., Carlson, H. C., Fleischman, J. R., et al. (1989). Rocket measurements within a polar cap arc: Plasma, particle, and electric circuit parameters. *Journal of Geophysical Research*, *94*(A6), 6692–6712. https://doi.org/10.1029/JA094iA06p06692

Wernik, A. W., Secan, J. A., & Fremouw, E. J. (2003). Ionospheric irregularities and scintillation. *Advances in Space Research*, *31*(4), 971–981. https://doi.org/10.1016/S0273-1177(02)00795-0

Yeh, K. C., & Liu, C.-H. (1982). Radio wave scintillations in the ionosphere. *Proceedings of the IEEE*, *70*(4), 324–360. https://doi.org/10.1109/PROC.1982.12313

Zettergren, M. D., & Hirsch, M. (2020). gemini3d/GEMINI-docs: KHI JGR paper. https://doi.org/10.5281/zenodo.3647589

Zettergren, M. D., & Hirsch, M. (2020). gemini3d/GEMINI-examples: KHI JGR paper. https://doi.org/10.5281/zenodo.3647584

Zettergren, M. D., & Hirsch, M. (2020). gemini3d/GEMINI-scripts: KHI JGR paper. https://doi.org/10.5281/zenodo.3647587

Zettergren, M. D., Semeter, J. L., & Dahlgren, H. (2015). Dynamics of density cavities generated by frictional heating: Formation, distortion, and instability. *Geophysical Research Letters*, *42*, 10,120–10,125. https://doi.org/10.1002/2015GL066806

Zhang, Q.-H., Ma, Y.-Z., Jayachandran, P. T., Moen, J., Lockwood, M., Zhang, Y.-L., et al. (2017). Polar cap hot patches: Enhanced density structures different from the classical patches in the ionosphere. *Geophysical Research Letters*, *44*, 8159–8167. https://doi.org/10.1002/2017GL073439